JGR Solid Earth

RESEARCH ARTICLE
10.1029/2026JB033929

Characterizing the Forearc Basement and Subducting Structures of the Northern Ecuadorian Margin

Arnaud Delsuc[1,2], Audrey Galve[2], Mireille Laigle[2], Andreas Rietbrock[1], Laure Schenini[2], Hans Agurto-Detzel[1], Alexandra Skrubej[2], Boris Marcaillou[2], Sandro Vaca[3], Annika Maier[1,4], and Michele Paulatto[5]

[1]Karlsruhe Institute of Technology, Geophysical Institute, Karlsruhe, Germany, [2]Université Côte d'Azur, IRD, CNRS, Observatoire de la Côte d'Azur, Valbonne, France, [3]Instituto Geofísico, Escuela Politécnica Nacional, Quito, Ecuador, [4]Risklayer GmbH, Karlsruhe, Germany, [5]Imperial College London, Earth Science and Engineering, London, UK

Key Points:

- We perform 2D Bayesian tomography of the northern Ecuadorian forearc margin updip of the 2016 M7.8 Pedernales rupture area
- 2D Vp models show a high vertical Vp gradient indicating the forearc basement as defined by MCS data and a reduced Vp at the margin wedge
- A low velocity anomaly in the subducting oceanic crust may be related to a fracture zone

Supporting Information:

Supporting Information may be found in the online version of this article.

Correspondence to:

A. Delsuc and A. Galve,
arnaud.delsuc@geoazur.unice.fr;
galve@geoazur.unice.fr

Citation:

Delsuc, A., Galve, A., Laigle, M., Rietbrock, A., Schenini, L., Agurto-Detzel, H., et al. (2026). Characterizing the forearc basement and subducting structures of the northern ecuadorian margin. *Journal of Geophysical Research: Solid Earth*, *131*, e2026JB033929. https://doi.org/10.1029/2026JB033929

Received 29 JAN 2026
Accepted 22 AUG 2026

Author Contributions:

Conceptualization: Arnaud Delsuc, Audrey Galve, Mireille Laigle, Andreas Rietbrock
Data curation: Arnaud Delsuc, Audrey Galve
Formal analysis: Arnaud Delsuc, Laure Schenini
Funding acquisition: Audrey Galve, Andreas Rietbrock
Investigation: Audrey Galve, Mireille Laigle, Andreas Rietbrock, Laure Schenini, Hans Agurto-Detzel,

Abstract

We present 2D P-wave velocity (Vp) models from the northern Ecuadorian subduction zone, north of the Carnegie Ridge. Data were collected during the HIPER2 3D wide-angle seismic experiment, both onshore and offshore. Key seismic profiles were manually picked to determine P-wave first-arrival times, which were used for a traveltime tomographic inversion based on a Bayesian approach. Interpreting these 2D Vp models jointly with existing multi-channel seismic (MCS) data reveals a high vertical Vp gradient (>0.85 km/s/km) consistent with the position of the forearc basement defined by MCS data, allowing us to map the basement along the margin. In addition, two notable low-velocity zones are identified. The first zone observed across all profiles within the inner margin wedge, is interpreted as resulting from rock fracturation and/or alteration near the trench. The second one present in the subducting oceanic crust, is characterized by a Vp reduction of 0.5–1.0 km/s relative to the surrounding areas and marks the northern termination of a previously identified trench-parallel velocities anomaly. As a possible origin of this distinctive anomaly, we propose the entry into subduction of an unmapped fracture zone (FZ), potentially reactivated by the increased plate bending due to the presence of the 2 km-high Carnegie Ridge. Three FZ are proposed as possible sources of this anomaly that would southwards extend fossil transform faults for 100–150 km.

Plain Language Summary

A detailed three-dimensional image of the seismic structure of the subduction interplate seismogenic zone is essential to understand the suspected relationships among fluids, faults, and seismic and aseismic slip behavior. To address this issue, we conducted an extensive seismic study at sea and on land in northern Ecuador, a region known for generating large earthquakes. We focused on key profiles and derived the corresponding seismic velocity structures, allowing comparison with the results of previous studies. Our results reveal a sharp increase in P-wave velocity at the boundary between the sedimentary layers and the crust beneath the Ecuadorian margin. Additionally, we identified two areas where P-wave velocity is lower than expected, likely reflecting more intense rock damage. The first area is identified in all four profiles and may reflect fractured or altered rocks near the trench. The second area, located within the subducted oceanic crust, may be associated with an unidentified fracture zone. Given the proximity of the Carnegie Ridge, which rises ~2 km high above the surrounding seafloor and exceeds 15 km in thickness, this inherited structure may have been reactivated by plate bending. Three extinct fracture zones could potentially account for this feature.

1. Introduction

Velocity structures in forearc domains of subduction zones provide valuable insights into rock properties, the structure and hydration levels on both blocks of the megathrust fault. These structural and petro-physical properties are recognized to play a significant role in the seismic activity, transient slips and deformation along the margin (Barnes et al., 2020; Bassett et al., 2022; Sallarès & Ranero, 2019; Wang & Bilek, 2014). Investigating them is then critical for a better understanding of the likelihood of megathrust earthquakes. The Ecuadorian margin is an ideal place to investigate the link between geological structures and seismic behavior. The megathrust fault reaches shallow depths very close to the coast and is known to have generated multiple large earthquakes in the last century, including the Mw 8.4–8.8 in 1906, the 7th largest earthquake ever recorded (Kanamori & McNally, 1982; Parra et al., 2016; Ye et al., 2016; Yoshimoto et al., 2017). Furthermore, the last major event, the 2016 Mw 7.8 Pedernales earthquake, occurred in an area where seismic swarms and aseismic

Alexandra Skrubej, Sandro Vaca, Michele Paulatto
Methodology: Arnaud Delsuc
Project administration: Audrey Galve, Andreas Rietbrock
Software: Arnaud Delsuc, Audrey Galve, Andreas Rietbrock, Annika Maier
Supervision: Audrey Galve, Mireille Laigle, Andreas Rietbrock
Visualization: Arnaud Delsuc, Audrey Galve, Mireille Laigle, Andreas Rietbrock
Writing – original draft: Arnaud Delsuc, Audrey Galve, Mireille Laigle, Andreas Rietbrock
Writing – review & editing: Arnaud Delsuc, Audrey Galve, Mireille Laigle, Andreas Rietbrock, Laure Schenini, Hans Agurto-Detzel, Alexandra Skrubej, Boris Marcaillou, Sandro Vaca, Annika Maier, Michele Paulatto

slip, including slow earthquakes and post-seismic slow slip, have been recorded (Agurto-Detzel et al., 2019; Chalumeau et al., 2023; Font et al., 2013; Rolandone et al., 2018; Vaca et al., 2018).

Numerous studies focused on the structure of the Ecuadorian margin at different scales to provide details of key seismic velocity structures and a regional P- and S-wave velocity model. Large scale 3D velocity models of the Ecuadorian margin have been proposed by León-Ríos et al. (2021) and Ponce et al. (2025). Further to the north, a 3D active seismic experiment was conducted with a dense OBS network and 10 land stations across the border with Colombia to precisely image the seismic structures in the source region of the 1958 Mw 7.7 earthquake rupture zone (García Cano et al., 2014). In the forearc domain, Hernández et al. (2020) presented a map of the sedimentary fill and topography of several sedimentary units offshore Ecuador, based on two way travel-time (TWTT) from multi-channel seismic (MCS) SCAN data set acquired by Petroecuador in 2009. In addition, a dense distribution of ocean-bottom seismometers (OBS), predominantly along 2D profiles, together with 2D multi-channel seismic (MCS) surveys were conducted to image the subduction fault and some key bathymetric features along the Ecuadorian margin (Agudelo et al., 2009; Gailler et al., 2007; Graindorge et al., 2004; Marcaillou et al., 2016; Sallarès et al., 2005).

However, there is a lack of local studies in the area of the Pedernales margin segment, where the 2016 M7.8 earthquake occurred, leaving the seismic structure of the crustal units of both plates along this margin segment largely unknown. To fill this data gap we conducted a high-resolution active offshore-onshore seismic experiment. In this study we focus on four selected profiles extracted from our survey: two trench-normal and two trench-parallel lines. Using first-arrival travel times from wide-angle seismic (WAS) shot recordings, we determine P-wave velocity (Vp) variations to image the margin structure, with the 2D inversion providing significant constraints despite the relatively low number of OBSs (4–9 per line) and their large spacing (>10 km). To mitigate the influence of the starting model required in standard linearized inversion schemes (e.g., FAST, Zelt and Barton (1998)) we use the Bayesian version of the tomographic code Tomo2D (Korenaga & Sager, 2012). We validate the results at shallow depths by a joint interpretation with available MCS data and present a first insight of first-order seismic velocity structures in the marine forearc and subducting oceanic crust. Our results contribute to a more detailed characterization of the Pedernales margin segment, located just north of the Carnegie Ridge.

2. Geodynamic Context

The North Andean margin is the result of long-term interaction between Nazca and South American (SA) plates. Currently, the 13–16 Ma old Nazca plate subducts beneath the North Andean Sliver with a rate of 4.7 cm/year in the N83°E direction (Nocquet et al., 2014) and has its origin due to the fragmentation of the Farallon plate into the Cocos and Nazca plate 23 Ma ago (Lonsdale, 2005).

Our study area is situated on the northern flank of Carnegie Ridge (CR) where the bathymetric imprint of CR near the trench fades away (Figure 1). The CR consists of a ~300 km wide and 14–19 km thick oceanic plateau that rises around 2,000 m above seafloor (Graindorge et al., 2004; Sallarès et al., 2005) and is the result of interaction between the Cocos-Nazca spreading center and the Galapagos hotspot (Sallarès & Charvis, 2003) about 1,000 km offshore Ecuador (Figure 1). Coastal uplift indicators, such as marine terraces, suggests that the CR has entered subduction beneath the North Andean margin (Collot et al., 2008; Pedoja et al., 2006) since at least the early Pliocene (Hernández et al., 2020; Ponce et al., 2025; Sallarès & Charvis, 2003). The Ecuadorian forearc domain formed during the Late Cretaceous through the accretion of oceanic terranes onto the South American margin, some of which show evidence of an oceanic plateau origin (Hernández et al., 2024), giving rise to the North Andean Block (Hernández et al., 2020, 2024; Jaillard et al., 2009; Reynaud et al., 1999). The igneous forearc basement is interpreted as being covered by volcanoclastic sediments and thick sedimentary basins that have developed since the Late Cretaceous (Hernández et al., 2020, 2024).

Previous geological and geophysical studies showed a highly segmented margin with a mainly erosional component up to 1°N (Collot et al., 2002; Font et al., 2013; Gailler et al., 2007; Hernández et al., 2020), and a northwards transition into an accretionary margin north of 2°N (Marcaillou, 2003). South of Punta Galera, from 2°S to 1°N, the Ecuadorian margin is predominantly erosional (Collot et al., 2008; Marcaillou et al., 2016) as a result of the subduction of the CR (Gailler et al., 2007; Graindorge et al., 2004) and Atacames seamount chain (0.4°N to 1°N). The latter is composed of a N-S trending line of four high seamounts 1–1.5 km high (Marcaillou et al., 2016) with the southernmost one located a few kilometers seaward from the trench (Figure 2). Additional evidence for already subducted seamounts is presented in Marcaillou et al. (2016) (Figure 2), which have been

10.1029/2026JB033929

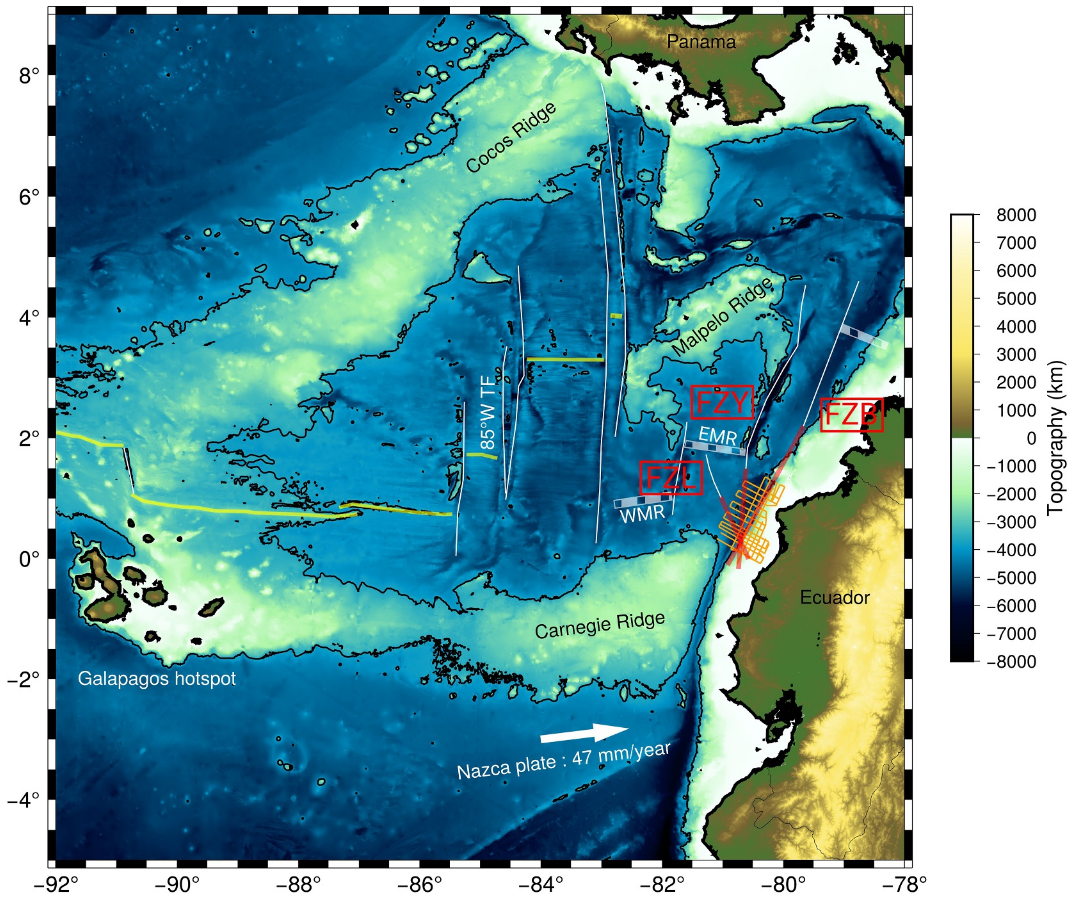

Figure 1. Bathymetric map and oceanic structures of the Panama basin off the coast of Ecuador. Yellow thick transparent lines correspond to spreading ridges (Hardy, 1991; Peirce et al., 2023) and white lines correspond to transform faults/fracture zones. Dashed white thick lines are extinct rifts (Hardy, 1991; Lonsdale, 2005). FZL (Fracture Zone from Lonsdale (2005)), FZY (Fracture Zone of the Yaquina graben) and FZB (Fracture Zone next to the Bueanaventura extinct rift) (red lines) indicate possible fracture zones that extend from identified transform faults to the Ecuadorian trench. The orange grid corresponds to the shots of the HIPER2 campaign. EMR stand for extinct Eastearn Malpelo Rift. WMR stand for extinct Western Malpelo Rift.

proposed as the cause of the deep Atacames re-entrant. North of Punta Galera, from 1°N to 3°N, previous studies highlighted standard oceanic crust thickness and seismic velocity structure (Agudelo et al., 2009; Gailler et al., 2007; García Cano et al., 2014). Several bathymetric features are present in the forearc in this area (Figure 2) such as numerous semi-circular scarps characterized with oversteepening slope (Camarones scarp) (Ratzov et al., 2010) and the trench-parallel Ancon fault running from 2.5°N (Collot et al., 2005, 2008, 2009) down to 1°N (Collot et al., 2025; Gonzalez, 2018). The oceanic crust offshore of this area presents major bathymetric features such as the Yaquina graben, interpreted as a fossil transform fault shifting the extinct Malpelo spreading center segment of the Nazca plate (Collot et al., 2009; Hardy, 1991; Lonsdale, 2005; Sallarès & Charvis, 2003) (FZY Figures 1 and 2). In addition, a fossil fracture zone has been identified by Lonsdale (2005) west of our study area (FZL Figures 1 and 2), and another one, the Minor fossil transform fault offsetting the Buenaventura extinct rift is located close to the trench, north east of the Yaquina graben (Hardy, 1991) north of our study area (FZB Figures 1 and 2).

3. Data Set

As part of the project “High resolution Imaging of the Pedernales Earthquake Rupture zone 2” (HIPER2), we deployed 43 Ocean Bottom Seismometers (OBS) in the rupture area of the 2016 Mw 7.8 Pedernales earthquake offshore Ecuador (Galve, 2022). The deployment started in January 2022 on land and in March 2022 at sea, using the French research vessel R/V L’Atalante. The OBSs were deployed on a rectangular grid with a station spacing

10.1029/2026JB033929

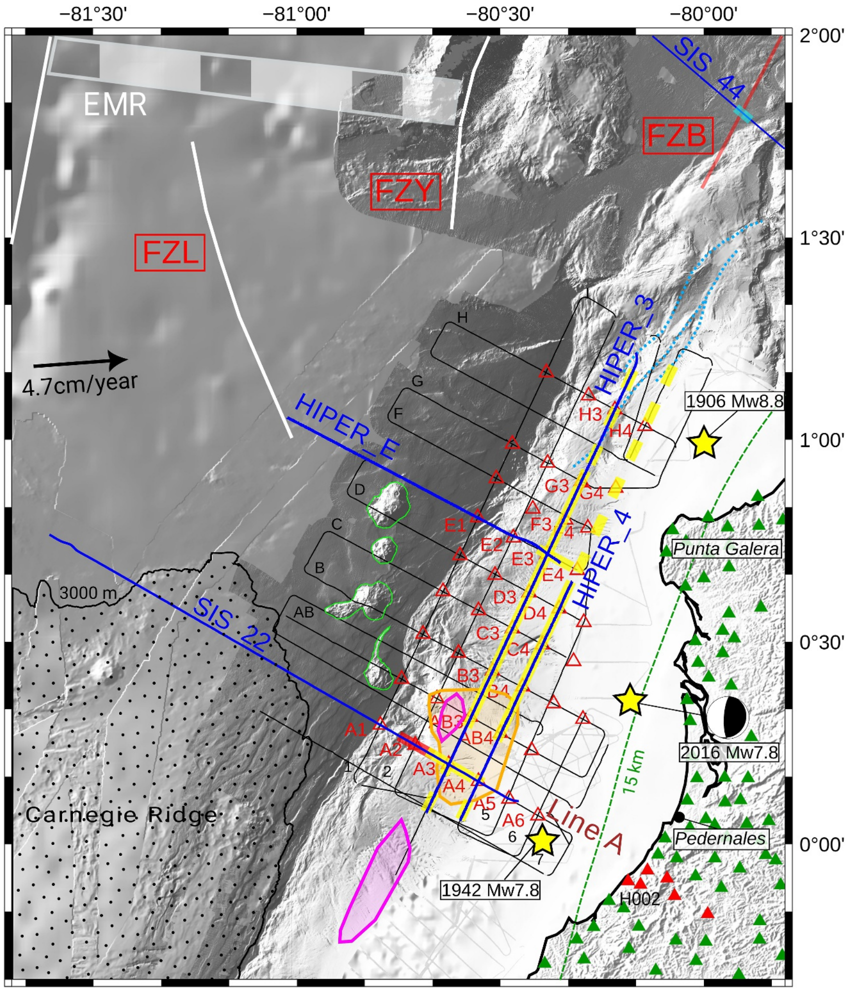

Figure 2. 3D grid acquisition of the HIPER2 marine campaign in Northern Ecuador and structural information from previous studies. Black lines correspond to the shots position for the wide-angle seismic acquisition, recorded by the OBS (red triangles) and land stations (green and red full triangles). Bathymetry is from Galve (2022). Black dotted area is the Carnegie ridge limited by the 3,000 m isobath. Light green contours are the bathymetric imprint of Atacames seamounts. White lines are fracture zones and the red line is the extension of the Minor fracture zone (Figure 1). Dark blue lines are multi channel seismic profiles from HIPER1 and the SISTEUR experiment (Collot, 2000; Galve, 2020). Light blue area corresponds to the presence of a graben in the oceanic crust seen on SIS44, trench parallel structure also seen on adjacent seismic lines (Collot et al., 2008). Yellow stars correspond to the mainshock associated with its GCMT focal mechanism for the Mw 7.8 2016 Pedernales earthquake, the Mw 7.8 1942 earthquake and the Mw 8.4–8.8 1906 Colombia-Ecuador earthquake (Kanamori & McNally, 1982; Parra et al., 2016; Sennson & Beck, 1996; Yoshimoto et al., 2017). Dashed green line is the 15 km isobath of the interplate. Blue dashed line corresponds to the position of the Ancon fault from Collot et al. (2008); Gonzalez (2018); Collot et al. (2025). Orange area is the position of the double peaked seamount from Marcaillou et al. (2016). Purple area is the position of A1 (northern area) and A2 anomaly (southern area) from León-Ríos et al. (2021). Thick red and yellow lines are respectively the position of the LVO and LVF zones on Lines A, 3 and 4.

of 10 km, covering the Ecuadorian forearc from the trench to the coast between 0°10′ South and 1°25′ North (Figure 2). To optimize spatial resolution beneath the shoreline we deployed 100 land stations (Figure 2). This amphibious network continuously recorded for 25 days. We used a 4990 cu.inch airgun array to acquire Wide Angle Seismic data (WAS) with approximately 14,000 shots and a spacing of 150 m (approximately every 60 s). All OBS internal clocks were synchronized with absolute GPS time before and after the deployment to correct for instrument drift. Typical drift rates were about 5 ms/day. For land stations, continuous GPS was used as time basis.

Here we present four selected profiles of the HIPER2 survey aiming at resolving the geometry of the forearc basement and the top of oceanic crust offshore northern Ecuador (Figure 2). Two profiles, Line A and Line E, are perpendicular to the trench and have 6 and 4 OBSs respectively. Line A also incorporates 6 land stations. The other two profiles, Line 3 and Line 4, are parallel to the trench, have 9 OBSs each and intersect with Line A and E at a distance of 20 and 30 km from the trench, respectively. Collocated MCS data were acquired during the HIPER1 campaign in 2020 along Line 3, Line 4 and Line E (Galve, 2020). Additional MCS data were acquired during the SISTEUR survey in 2000 (Collot, 2000) which collected several MCS profiles along the Ecuadorian subduction zone, including one along the western part of Line A.

4. Arrivals Identification and Picking

First arrivals were manually picked on all OBS sections using the Shearwater Reveal software package. In total, 11870 high quality first arrivals were picked at the hydrophone channel (with a corner frequency of 2 Hz) and at the vertical component of the OBS geophones (with a corner frequency of 4.5 Hz). Different filters were applied to maximize the signal-to-noise ratio (SNR) of first arrivals. One with a bandpass between 0.05 and 80 Hz to suppress very low and high frequency noise components and two more restrictive filters with a bandpass between 2.5 and 16 Hz and between 2.5 and 8 Hz. Different uncertainty classes were assigned to each pick ranging from 0.05 to 0.15 s (Figure 3), depending on the filter used and picking accuracy. The three different filters are presented in the Supporting Information S1 on one OBS from profile A (Figure S1 in Supporting Information S1). For OBSs located on the oceanic crust (e.g., A1 in Figure 3a), Pg arrivals (refracted waves in the crust) have an almost constant apparent velocity of about 7.0 km/s, whereas for OBS on the continental margin (e.g., C3 in Figure 3b), first arrivals at close offsets have an apparent velocity between 4.0 km/s to 6.0 km/s. At longer offsets, first arrivals also have a constant apparent velocity of about 6.0–7.0 km/s. At far offset the apparent velocity is higher than 7.0 km/s and reaches up to 8.0 km/s in some OBS sections. Few PmP phases (reflected waves on the Moho) could be identified and picked on line 3 (Figure 3b). To help identifying interplate reflections (PiP) in OBS sections, we incorporated the MCS-derived reflector as a floating interface in our tomographic model and forward-modeled the reflected waves (Figure 3). On OBS sections, PiP phases, amid complex patterns, are hard to distinguish, and those matching the MCS interplate (orange line, Figure 3) are difficult to pick. With few crossing rays (Figure S14 in Supporting Information S1), the picks are insufficient to reliably constrain the interplate topography from the limited OBSs per line. Nevertheless, the reflected waves in the OBS data align well with those from the MCS-derived interplate reflector. Identification and inversion of PiP and PmP phases will benefit from the 3D view that is beyond the scope of our manuscript. For land stations, we used a different processing sequence to improve SNR and assigned larger pick uncertainties of 0.2 s (Figure S2 in Supporting Information S1). This processing sequence includes debias, whitening, application of a Butterworth filter and amplitude equalization (automatic gain control).

5. Method: Bayesian Approach of Tomo2D

The joint refraction and reflection tomography method of Korenaga et al. (2000), specifically its Bayesian formulation (Korenaga & Sager, 2012), was applied to our manually picked P-wave first arrivals to obtain 2D P-wave velocity models. This allows us to avoid the selection of specific values for the input parameters and the choice of a starting model. Instead, it draws from a priori ranges to generate numerous initial velocity models, and employs adaptive importance sampling to iteratively refine the starting model selection over the course of the inversion. We use the same velocity inversion mesh structure for all profiles with a horizontal node spacing of 1 km and a vertical node spacing of 0.2 and 0.5 km in the upper 2 km and from 2 to 40 km, respectively.

We selected a priori ranges corresponding to the following thirteen input parameters: the velocity at the top of the upper, middle and lower layer for the initial velocity model (L_1, L_2, L_3), the thickness of the upper and middle layer (HL_1, HL_2). For smoothing constraints we use the horizontal and vertical correlation length at the top of the upper layer ($L_{h,0}$, $L_{v,0}$), the thickness of the upper and middle layers over which different correlation length values are applied (HCL_1, HCL_2), the ratios used to compute correlation lengths in the middle, lower layer (rlh, rlv) and the depth kernel weighting (w) and Z_m the initial depth of the starting reflector the inversion for profiles inverting for the Moho topography.

The a priori ranges of the input parameters vary between profiles due to structural differences and are listed in Table 1. L_1, L_2, L_3, HL_1, HL_2 and Z_m are responsible for building the starting models (Figure S3f in Supporting Information S1). For Lines 3 and 4, they were chosen to match an average 1D model obtained from a first inversion using broader a priori ranges. This was done to allow the algorithm to explore the full range of

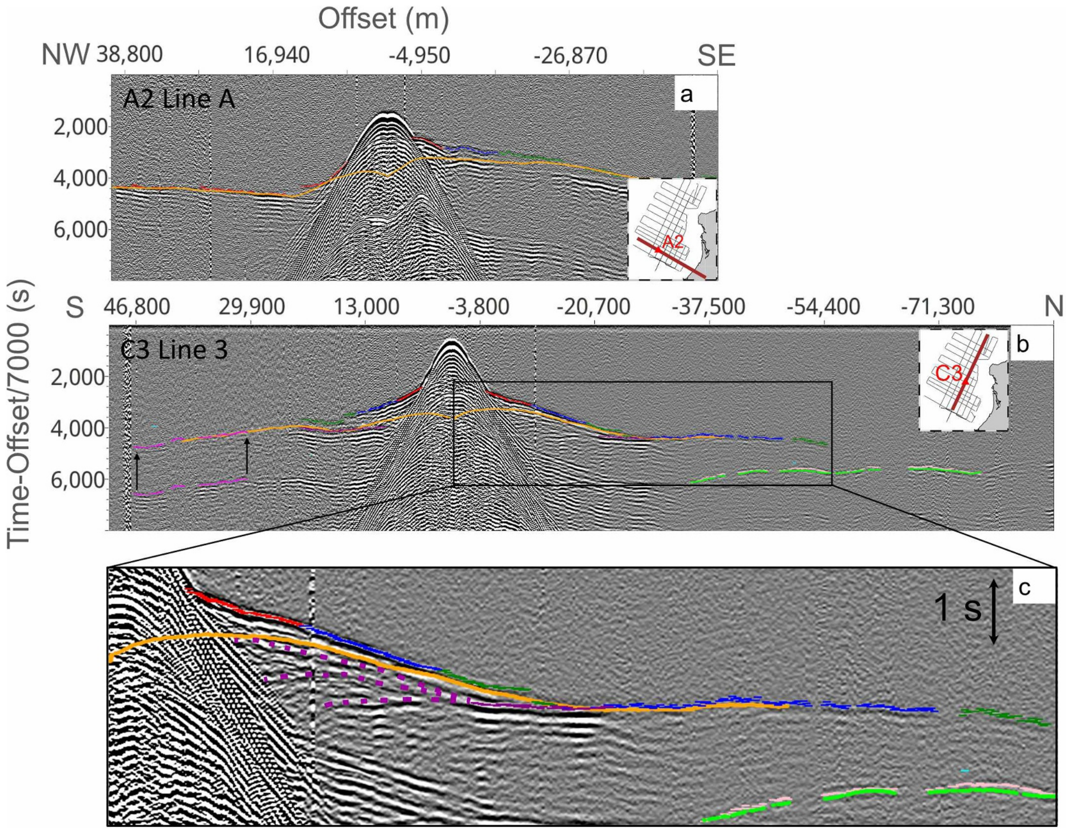

Figure 3. Offshore-onshore seismic data (a) Section for OBS A2 on Line A (perpendicular to the trench). A bandpass filter of 2.5–16 Hz and a velocity reduction of 7.0 km/s have been applied. (b) Section for OBS C3 on Line 3 (parallel to the trench). A bandpass filter of 2.5–16 Hz and a velocity reduction of 7.0 km/s have been applied. (c) Zoom of the OBS C3 section. First arrivals are represented in red, blue and green corresponding respectively to an uncertainty of 50, 70 and 150 ms. Magenta first arrivals were manually picked on the multiple and time-shifted prior to inversion, with an assigned uncertainty of 150 ms. PmP phases are represented in pink with an assigned uncertainty of 70 ms. Calculated PmP traveltime are represented in green. Predicted PiP are represented in orange on (a, b and c). Purple arrivals represent the picked PiP phases for the forward model in Figure S14 of Supporting Information S1. Dashed purple line represent potential PiP arrivals.

physically valid models. On Line 3, L_1 corresponds to the velocity just below the seafloor representing sediments. L_2 represents the velocity at the top of the oceanic crust and L_3 is set to correspond to the velocity at the Moho interface. We choose HL_1 and HL_2 accordingly to correspond to the thickness of the forearc and of the oceanic crust. As Line 4 is 10 km further east from the trench, the assigned velocities differ from Line 3. L_2, L_3, HL_1 and HL_2 are set to correspond to velocity gradient changes shown by the average 1D velocity model with no obvious link to geological changes.

As Line A and E are perpendicular to the trench, it is more difficult to select a 1D velocity model to describe the active margin along the profile. We choose a priori ranges that encompass 1D Vp models of the regional oceanic crust velocities (García Cano et al., 2014) as well as 1D Vp models in the Ecuadorian margin (García Cano et al., 2014; Graindorge et al., 2004). Figure S3 in Supporting Information S1 shows the corresponding mean starting model for each line as well as the compilation of all used initial 1D Vp models.

5.1. Inversion Strategy

We performed the inversion following the framework presented in Figure 4. First we have an initialization part (i0 Figure 4) where M sets of parameters are randomly generated from their a priori ranges. As described in the previous paragraph, M different initial 1D velocity models are then built using these drawn parameters (Step 1, Figure 4).

Table 1
Parameter Ranges for Different Seismic Lines

Effective parameter	Range for line A and line E	Range for line 3	Range for line 4
L_1: Velocity top of upper layer	1.7–4	1.7–3	1.7–3
L_2: Velocity top of mid-layer	3–6	4–6.5	4.0–5.5
L_3: Velocity top of lower layer	6–8	6.5–8	6–7
HL_1: Upper layer thickness for starting model	1–4	5–10	2.5–5.0
HL_2: Middle layer thickness for starting model	3–6	7–20	12.0–14.0
$L_{h,0}$: Horizontal CL at $z = 0$	2–20	2–20	2–20
$L_{v,0}$: Vertical CL at $z = 0$	1–3	1–3	1–3
rlh: factor to calculate deeper horizontal CL	1–3	1–3	1–3
rlv: factor to calculate deeper vertical CL	1–3	1–3	1–3
HCL_1: Thickness of upper layer for CL	3–9	3–9	3–9
HCL_2: Thickness of middle crust for CL	15–25	20–30	20–30
$\log(w)$: log of depth kernel weighting	−2 to 2	−2 to 2	−2 to 2
Z_m: Initial depth of the reflector	–	15–30	–

Each of these models are then inverted, and the corresponding normalized data misfit is calculated (χ^2/N) (step 2, Figure 4). The data misfit is then represented as a function of the input parameters (step 3, Figure 4), allowing subsequent parameter selection to be guided rather than randomly sampled (step 4, Figure 4). The next step enters the iterative part of the code by running the inversion and collecting output model as well as χ^2/N and a new computed parameter called R (step 5, Figure 4). This parameter R is a model measure that represents the average relative deviation of the model from a 1-D reference velocity model using the following equation (Korenaga & Sager, 2012):

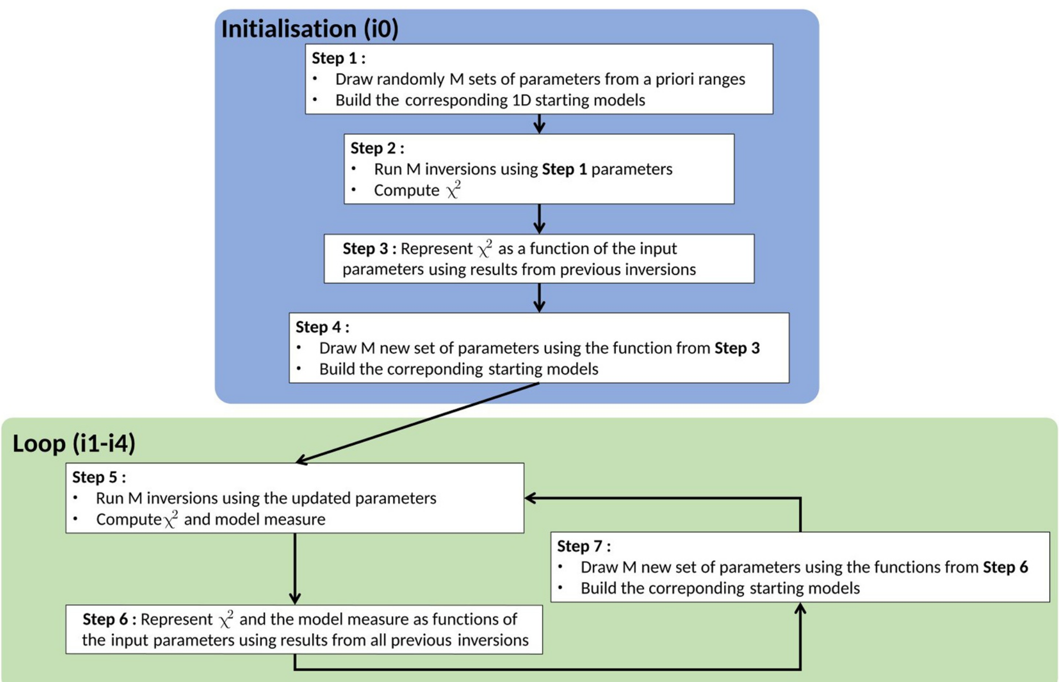

Figure 4. Overall framework of Bayesian approach of Tomo2D following the approach of Korenaga and Sager (2012).

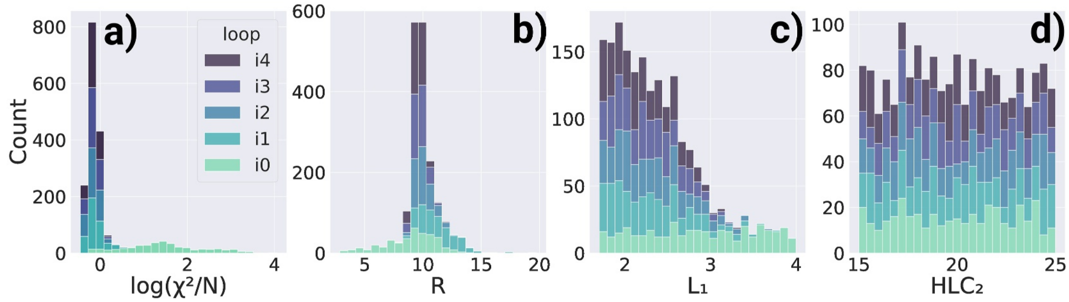

Figure 5. Distribution of effective parameters through iterations. Blue shades correspond to the associated iteration. (a) log of normalized χ^2, (b) model roughness (R), (c) initial velocity for the top of the upper crust (L_1), (d) thickness of the lower crust for the correlation length (HLC_2).

$$R \equiv \left(\int_\Omega \left(\frac{V(x,z) - V_{\mathrm{ref}}(z/h(x))}{V_{\mathrm{ref}}(z/h(x))} \right)^2 dx\,dz \Big/ \int_\Omega dx\,dz \right)^{1/2} \times 100, \tag{1}$$

with Ω, the entire crustal domain, h(x), the crustal thickness, and Vref, a horizontally averaged velocity profile. It is used in Korenaga and Sager (2012) and Yuan et al. (2020) as a possible measure of the overall roughness of the model. Consequently, this parameter is used to discard velocity models that display small-scale, high or low velocity anomalies considered geologically unrealistic.

In step 6, R is represented as a function of input parameters and used in addition with the χ^2/N function to select input parameters from a priori ranges in all subsequent loops (step 7, Figure 4). The two functions are updated at the end of each loop in step 6 before a new selection of a set of input parameters in step 7 (Figure 4).

5.2. Adapting the Bayesian Approach of Tomo2d to Our Data Set

For each profile, 1920 individual inversions were performed consisting of $M = 384$ individual inversions for each loop. Each inversion has a maximum of 20 iterations. We chose to conduct four loops (i1 to i4) in our inversion scheme (Figure 4) in addition with the initialization (i0) similarly to previous studies (Korenaga & Sager, 2012; Yuan et al., 2020). Using more than four loops did not significantly change the results but only increased the computing cost as similar input parameters are already drawn for the last two loops highlighting a stable choice of parameters after the first loops (Figure 5).

Previous studies based on the Bayesian version of tomo2D highlight that a different threshold value of R is needed in the iterative process depending on the studied object (Korenaga & Sager, 2012; Yuan et al., 2020). Yuan et al. (2020) showed, in their study of the Greenland passive margin, that achieving both a good data misfit $\left(\chi^2/N \approx 1\right)$ and a low R is difficult. They emphasized that each data set requires an R value suited to its acquisition parameters, raising R from 5, a value used for an oceanic plateau (Korenaga & Sager, 2012), to 8, to obtain acceptable misfits on their study of a passive margin (Yuan et al., 2020). In our case, given the higher complexity due to the tectonic overlap of two plates in this active margin, we used R values of 10 (trench-normal) and 9 (trench-parallel). Lower R values led to failure, as no suitable parameters could produce optimal models.

5.3. Extracting Results

The overall distribution of input parameters, $\log\left(\chi^2/N\right)$ and R as a function of the number of loops (i0-i4) shows the effect of the adaptive importance sampling applied in step 7 (Figure 4). Figures 5a and 5b show a distribution of $\log\left(\chi^2/N\right)$ and R localized below 0 and 10 respectively after the initialization (i0). This highlights how well R and χ^2/N are modeled as functions of input parameters in step 6 (Figure 4) generating much more optimal models $\left(\log\left(\chi^2/N\right) \approx 0 \text{ and } R < 10\right)$ after the i0 and beyond. Regarding the input parameters, a localized distribution after i0 (Figure 5c) indicates an input parameter that directly affects the data misfit and/or R, which is selected in a restricted range by the algorithm during step 7 (Figure 4). On the contrary, a homogenous distribution through loops such as HCL_2 (Figure 5d) shows a parameter that has little effect on data misfit and R. In this case, this is due to the lack of constraint on the output model at the depth at which HCL_2 is applied. The complete distribution of all input parameters for each Lines is available in (Figures S4–S6 in Supporting Information S1).

An output model is considered optimal for $\chi^2/N \approx 1$ and $R < 10$ for Line A and E, and for $\chi^2/N \approx 1$ and $R < 9$ for Line 3 and 4. To construct the final output model we average all optimal models that have been produced after the initialization. To avoid the selection of overfitting models, we extracted from each successful run the model with χ^2/N values the closest to 1. The mean of all optimal output velocity models ($\chi^2/N \approx 1$ and $R < 10$ or $R < 9$) for each line is then presented as the final output velocity model. Depending on the line, a different number of optimal models were generated with 791 optimal models for Line A, 1162 for Line E, 1047 for Line 3 and 1254 for Line 4. All the final output velocity models have an RMS between 60 and 95 ms.

5.4. Spatial Resolution

To estimate the spatial resolution of our models, we conducted checkerboard tests with 10% amplitude anomalies of three sizes: small (SA, 5×2.5 km), medium (MA, 10×5 km), and large (LA, 20×10 km). The results define a resolution mask to highlight well-recovered regions for each test (black dotted line in Figure 6). Checkerboard results are also compared with uncertainty estimations based on the standard deviation across the optimal models.

On Line A, the area below the OBS (2–52 km landward of the trench) is well resolved in shape down to 10 km depth for MA and LA, and 7 km for SA. However, recovered amplitudes are lower especially in the uppermost kilometer (∼50% of initial anomaly). Anomalies between land stations and OBS are poorly resolved, except for LA down to 10 km. Below the land stations, where we only have receivers and no shots, LA are partially recovered in shape but with ∼70% of the initial amplitude. On the marine side of the line, beyond the last OBS, the absence of crossing raypaths causes a reduced recovery of SA and MA. Line E shows similar results over a narrower range (−10 to 28 km landward of the trench) due to fewer OBS and no land stations. Recovered amplitudes on this line for LA and MA are 90% and 70%, respectively.

The resolution is better along trench-parallel profiles due to the increased profile length and better OBS coverage. On Line 3 (Figure 6c), LA are well resolved down to 10 km along the profile and to 17 km between 35 and 100 km. MA are recovered to 10 km depth between 30 and 95 km, while SA are best resolved to 7 km depth but show amplitude reduction and smearing effects between positive anomalies. SA and MA are not well resolved in the northern section of Line 3 due to sparser OBS coverage. On Line 4 (Figure 6d), MA are well recovered from 10 to 80 km down to 10 km depth, with another patch at 100–140 km down to 5 km depth. SA are only resolved between 15 and 63 km down to 5 km depth and between 110 and 135 km down to 2 km depth with ∼30% of the initial amplitude in the first ∼2 km depth. LA are generally well recovered down to 10 km, reaching 20 km between 40 and 100 km but with smaller amplitudes (∼50%). The low-resolution zone between 70 and 110 km results from shot restrictions during the acquisition, largely affecting SA and MA recovery.

To assess uncertainties, we computed the standard deviation across all optimal output models (Figure S8 in Supporting Information S1). Below the OBS, uncertainty is very low (<0.1 km/s, <3%) down to 3 km on dip-lines and 5 km on strike-lines. However, areas with poor OBS coverage, such as the oceanic crust on dip-lines, show higher uncertainties (>0.3 km/s, >4%). Compared to checkerboard tests, well-recovered areas generally correspond to regions of low uncertainty, where the uncertainty does not exceed the recovered anomaly amplitude, except for certain local anomalies. However, not all regions with low uncertainty are well recovered in the checkerboard test, particularly at depths greater than 10 km, where uncertainty is below 3%, yet anomalies SA, MA, and LA remain unrecovered. This behavior was highlighted by (Korenaga & Sager, 2012) who pointed out that the low uncertainties at greater depths are largely due to the influence of smoothing constraints and the use of initial velocity models bounded by geologically reasonable values. In the following, we chose to apply the LA mask to Figures 7 and 8 to show unresolved areas in half-transparency. We chose the LA mask over SA and MA mask to be the more inclusive and discard only part of the model that are not resolved for any size of anomalies.

6. Results

Here we present our analysis of four profiles which provide the tomographic Vp structure of the oceanic crust at the trench, and of the marine part of the inner margin wedge (the first 30 km of the forearc domain) down to a depth of 10–12 km (Figure 7).

10.1029/2026JB033929

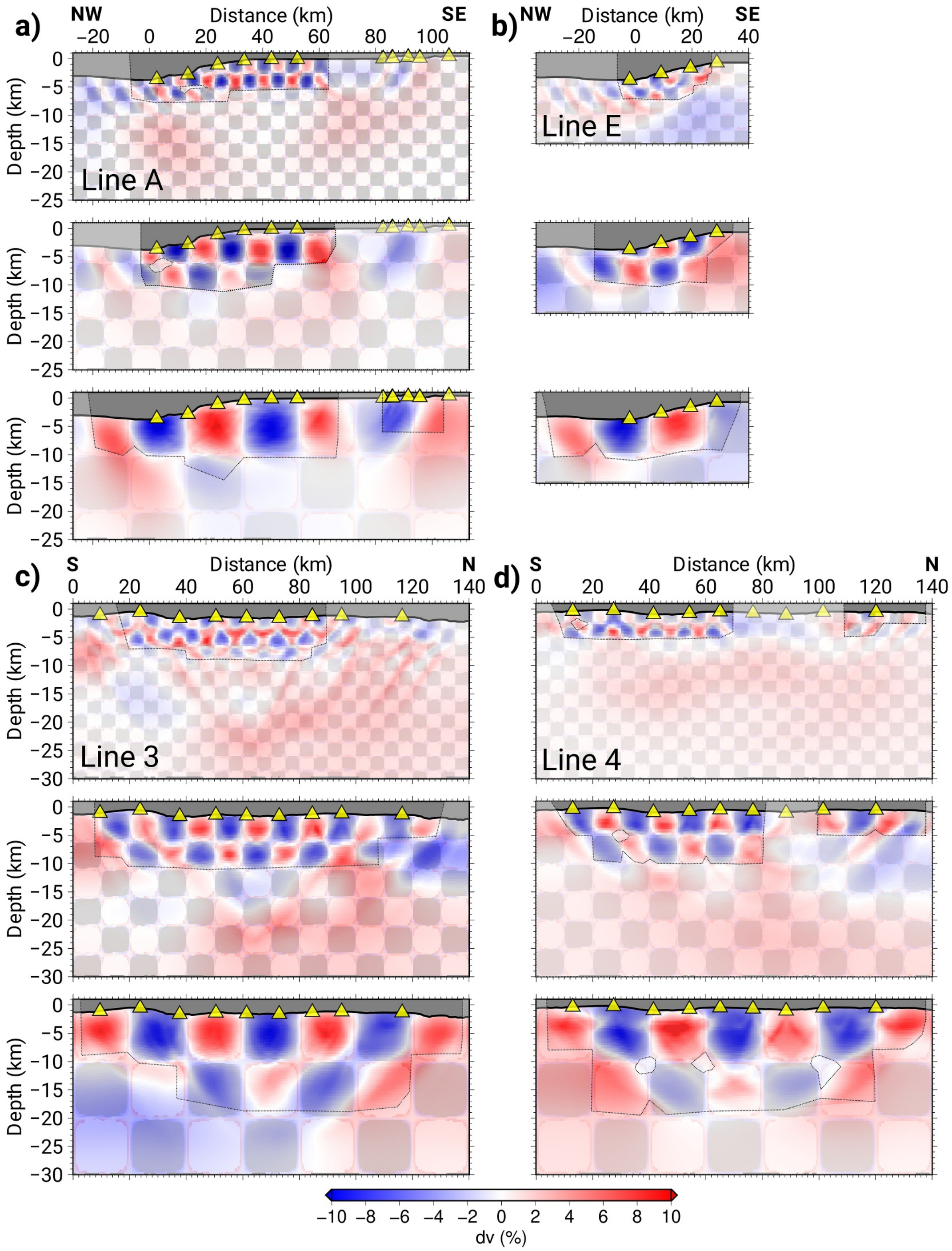

Figure 6. (a–d) Checkerboard test on Line A, E, 3 and 4 respectively. For each profile we run a checkerboard test with 5 × 2.5, 10 × 5 and 20 × 10 km anomalies. Input models with alternated positive and negative anomalies of 10% of the initial starting velocity model are visible as a transparent black and white layer on top of recovered models. Black dotted lines mark the end of the resolved area (shape of anomalies).

We also use MCS profiles from previous studies providing independent constraints on the basement topography of both the oceanic and upper plates. For Line A, we use the MCS profile SIS22 (Sisteur survey, Collot (2000)), which covers the western half of the line (Figure 2). We refer to the MCS interpretation of Marcaillou et al. (2016), updated by cross-checking with the 2009 Ecuadorian industrial SCAN data set acquired along the margin (see Collot et al., 2022; Hernández et al., 2020). This led into a slightly shallower location of the forearc

10.1029/2026JB033929

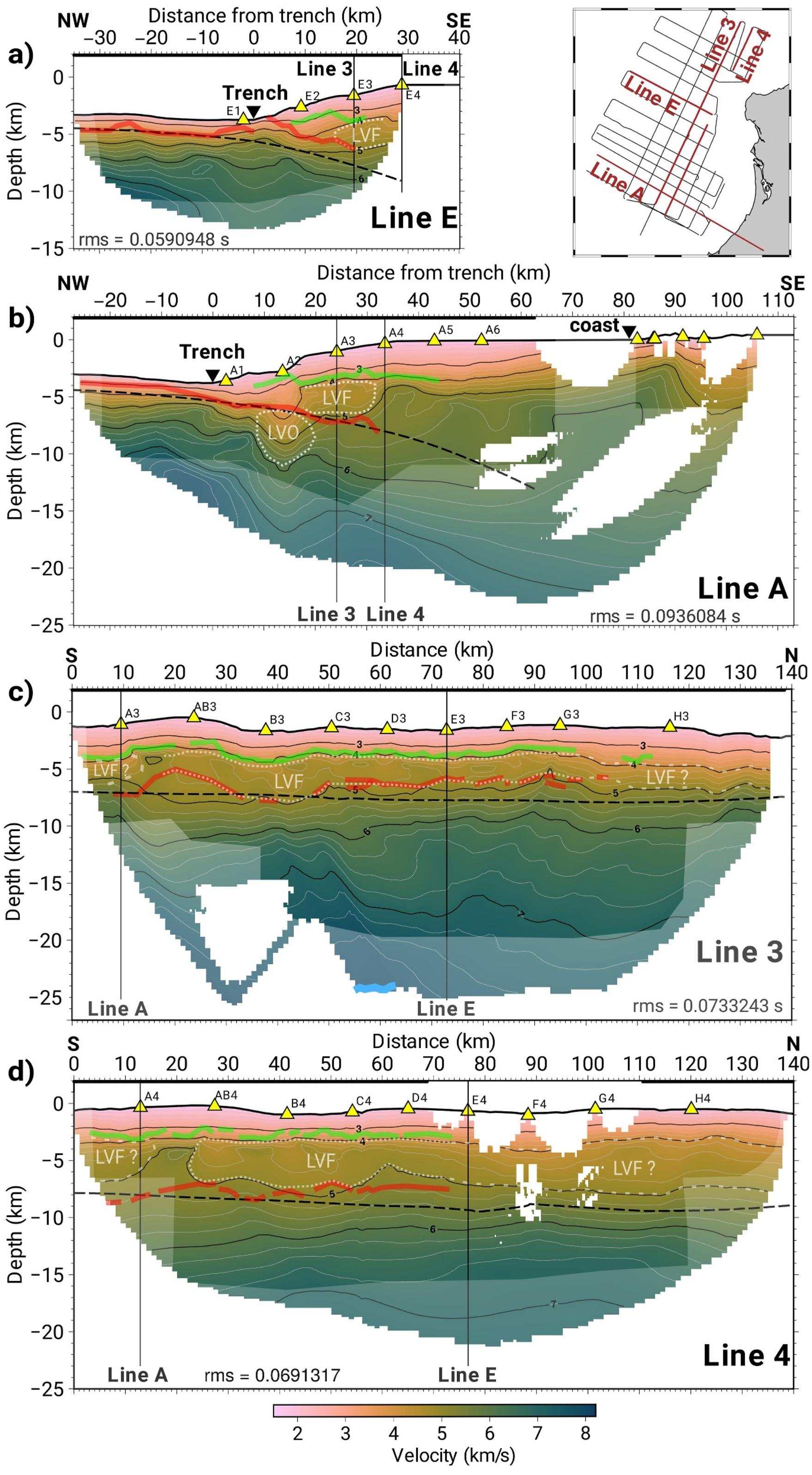

Figure 7.

basement, which follows the base of the highly reflective lower sedimentary layer's top (the ls unit in Marcaillou et al. (2016)). For lines E, 3 and 4 which have been collected during HIPER1 cruise (Galve, 2020), we provide here a preliminary interpretation of the forearc basement and interplate reflectors on the coincident MCS profiles (HIPER E, 3 and 4, Figure 2).

To avoid differences arising from a chosen velocity model during the depth migration of MCS data set, we use the two-way travel-time (TWTT) data and convert them to depth using our Vp model. We then obtain the reflector position onto the depth-domain velocity model. Figure 7 shows the reported basement topography together with our new velocity models.

We use the vertical velocity gradient to highlight velocity variations and seismic structures (Figure 8), following previous works (Acquisto et al., 2022; Evain et al., 2013; Seher et al., 2010). Finally, we also incorporate the slab topography from the 3DVM model of Font et al. (2013), which is based on the relocated seismicity. This 3DVM model better fits at shallow depths with the oceanic basement imaged on the available MCS profiles (HIPER E, 3 and 4 Galve (2020) and SISTEUR 22 Collot (2000)), than Slab 1.0 and 2.0 (Hayes et al., 2012, 2018) (Figure S10 in Supporting Information S1).

In the following we focus on the most prominent features of our velocity models. We describe distance landward to the trench using DLT acronym in the rest of the paper.

6.1. Forearc Basement of the Inner Margin Wedge

On Line A (perpendicular to the trench) the first few kilometers of the margin slope after the trench belong to the outer margin wedge. It is 8 km wide in line A and much narrower (<4 km) in line E (also perpendicular to the trench) due to the presence of an oceanic-high entering the trench (Figures 7a and 7b). Further landward, within the frontal part of the inner margin wedge toe (from 8 to ∼17 km DLT), the MCS acoustic forearc basement in Line E (HIPER E profile (Galve, 2020)) is strongly affected by numerous faults as seen for example, in line A (SIS22 profile, see Figures 2 and 3 of Marcaillou et al. (2016)). The forearc basement in this area corresponds to the isovelocities of 2.7–3.0 km/s that increase landwards up to 3.5–4.0 km/s. These values are similar to previous studies further south, at 1.5°S of latitude, where the Carnegie ridge enters the trench (Gailler et al., 2007; Graindorge et al., 2004). The forearc basement depth increases landwards on line A, from 0.5 to 1.0 km below sea-bottom (at 10 km DLT) to 3–3.5 km (at 45 km DLT).

On Line 3 (parallel to the trench), the basement is coincident with the ∼4.0 km/s contour from A3 to F3 over a 85-km-long distance, and oscillates around depths of 3 and 4 km. North of G3 the basement in MCS (HIPER 3 profile (Galve, 2020)) becomes discontinuous, with sparse reflectivity south of H3. On Line 4, the basement is shallower, around 2.5 km depth with 0.5 km high variations and oscillating between the 3 and 4.0 km/s isovelocity contours. The forearc basement is characterized by a layer with a high vertical Vp gradient higher than 0.85 km/s/km (HVVG) over most of the study area (Figure 8). Extracted 1D Vp models referenced to the seafloor at different distances from the trench, along with vertical Vp gradient values, highlight a 1.0–1.5 km thick HVVG layer (Figure 9). The maximum value of this gradient matches the acoustic reflector of the forearc basement from MCS HIPER 3 and 4 profiles (Figures 8c and 8d and 9). In the dip-lines, this HVVG layer begins ∼ 15 km DLT (about 10 km from the inner margin wedge toe, between A2/E2 and A3/E3) and extends more than 50 km DLT on line A (between A5 and A6, Figure 8a), and to the end of line E (up to E4, ∼30 km DLT).

In the strike-lines, it extends over 90 km on Line 3 (from A3 to G3), and over 130 km on Line 4 with a gap of 40 km in the middle (from south of E4 to north of G4), due to poorer spatial resolution at shallow depth caused by the absence of shots (Figures 2 and 6d). In the Northern part of Line 3 (>100 km model distance), the HVVG terminates where the basement reflector from the MCS HIPER 3 profile ends (Figure 8c). On Line 4, we cannot

Figure 7. Mean of all optimal output models for Line E (a), Line A (b), Line 3 (c) and Line 4 (d) with their respective RMS. Two masks have been applied to each line. First, a white mask was applied to the area devoid of raypaths, using the null value of the derivative weight sum parameter (DWS). The second is a transparent mask corresponding to the large anomaly mask highlighted in Figure 6. Dashed black line represents the interplate from Font et al. (2013). Bold black line on the *X* axis represents the active seismic shots that have been picked along the line. Doted white lines outline the areas of the LVF (Low Velocity area in the Forearc crust) and LVO (Low Velocity anomaly in the Oceanic crust). Dashed white lines outline the potential extension of the LVF. Green and red lines are the forearc and the oceanic basement identified in the MCS (HIPER E, 3 and 4 Galve (2020) and SISTEUR 22 Collot (2000)). The blue line indicates the portion of the Moho constrained by crossing raypaths.

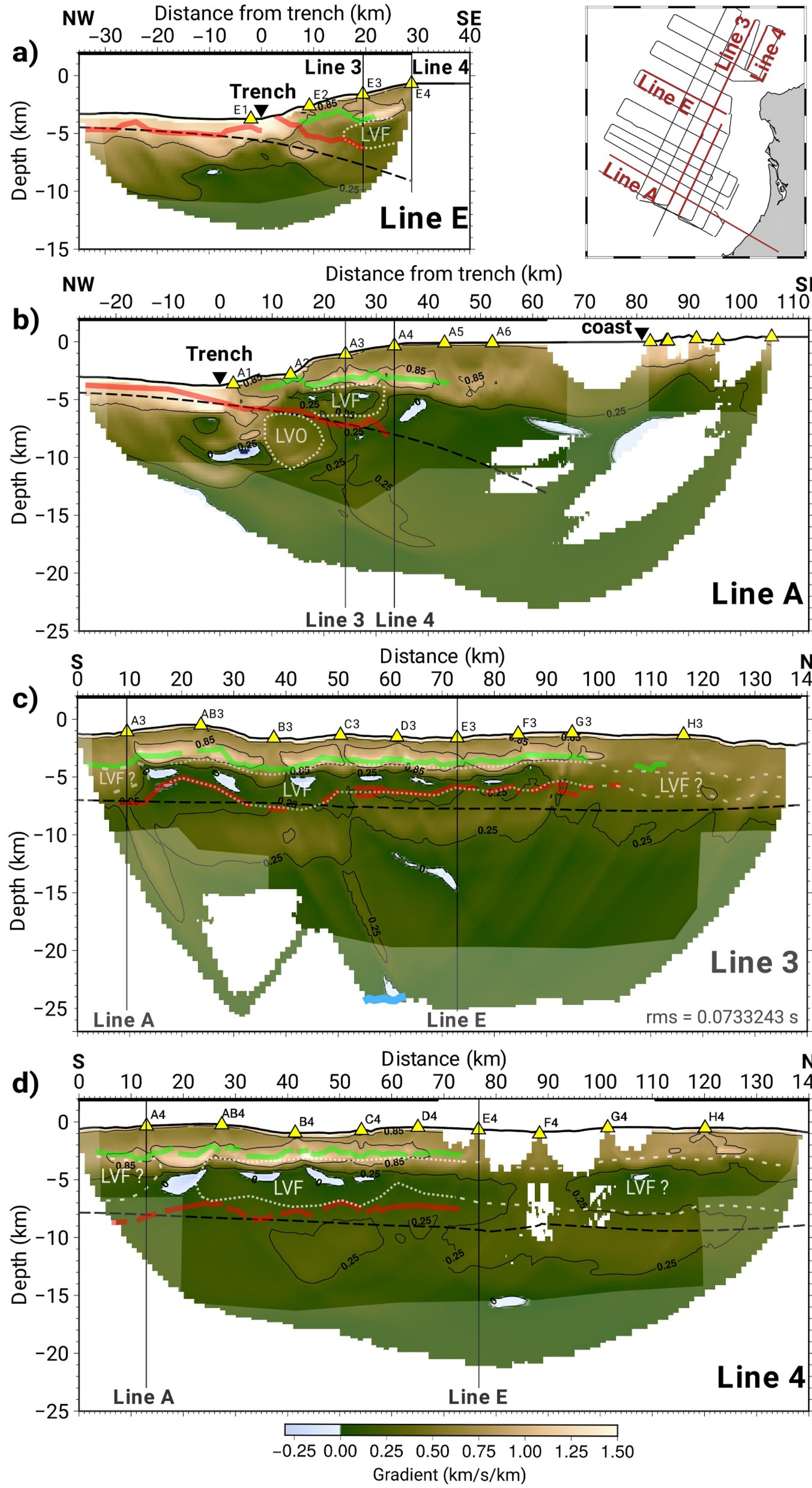
a)
NW
Distance from trench (km)
SE
Depth (km)
Line 3
Line 4
Trench
LVF
Line E
b)
NW
Distance from trench (km)
SE
coast
Trench
LVF
LVO
Depth (km)
Line 3 Line 4
Line A
c)
S
Distance (km)
N
LVF ?
LVF
Depth (km)
Line 3
Line A
Line E
rms = 0.0733243 s
d)
S
Distance (km)
N
LVF ?
LVF
Depth (km)
Line 4
Line A
Line E
Gradient (km/s/km)
Line 3
Line 4
Line E
Line A

Figure 8.

correlate the termination of the acoustic basement at 75 km model distance with structural changes since MCS HIPER 4 profile stops there (before line E).

6.2. Upper Plate's Crust and Low Velocity in the Forearc Crust (LVF)

The forearc igneous crustal part lies above the interplate (Figures 7a–7d and 8a–8d). The interplate is identified down to depths of 7–10 km on the four MCS HIPER E, 3, 4 and SIS22 profiles (e.g., Figure 3 in Marcaillou et al., 2016), and is extended further by the slab model of Font et al. (2013).

In the southern part of our study area, on Line A, the forearc crust thickness laterally increases above the dipping top of the slab, from 3 km at 20 km DLT (A3) to 5 km thick at 32 km DLT (A4), with Vp above the interplate ranging from 5.2 km/s to 5.4 km/s (Figures 7b and 9b). In the central part of our study area, Line E highlights a 2 km thick forearc crust with similar velocities at 20 km DLT (E3).

Strike-lines reveal the trench-parallel lateral extension of these results at a distance of 15–20 km DLT for Line 3, and 25–30 km DLT for Line 4. Line 3 highlights a 2–3.5 km thick forearc crust from C3 to south of G3, with velocities of ~4.0 km/s at the top and 4.7–5.0 km/s above the interplate. In the southern part of Line 3, the forearc crust is affected by the presence of a subducted seamount that thins the forearc crust to 2 km at its peak below AB3 according to MCS profile SIS 22 (Marcaillou et al., 2016). The only notable change in Vp is above the southern flank of the seamount. However this anomaly is outside our resolved area considering its size (small anomalies, Figure 6c). As a result, the two km of forearc crust located above this subducted seamount do not have a distinct Vp signature. North of G3, Line 3 displays a different Vp structure with an almost constant velocity gradient and a Vp value of 5.2 km/s at the interplate. However this area has a sparser OBS coverage which could affect the Vp velocity structure.

Line 4 shows a thicker forearc crust than Line 3. According to the MCS acoustic reflector from profile HIPER 4 (Galve, 2020), the mean thickness value is of ~4 km in the southern half of the line, from A4 to E4 (Figures 7d, 8d and 9) with velocities ranging between 3.2 and 5.2 km/s. In this area, the profile exhibits changes in depth of the 4.8–5.0 km/s iso-velocity contours, which become shallower at 20, 35 and 60 km model distance. A sharp lateral change in depth of the 5.0 km/s contour on Line A occurs at the crossing point with Line 4.

We define a low velocity in the forearc crust (LVF) within the toe of the inner margin wedge on Lines A and E (Figures 7a and 7b) at 15–30 km DLT. This zone, located just above the slab interface, is characterized by forearc crustal velocities of <5.0 km/s. Its well resolved segment extends along-trench on Line 3 over a ~ 80 km long portion, from 7 km north of Line A up to where the acoustic basement reflector ends (beyond 97 km model distance, Figure 7c). On Line 4, it extends from 10 km from Line A over a ~ 50 km long portion. Both lines cross higher velocity forearc margin on their southern part.

6.3. Low Velocity Anomaly in the Oceanic Crust (LVO)

In global compilations of oceanic crust, Vp increases from 3.0–5.5 km/s at the top of the crust to 6.8–7.2 km/s at the Moho (Christeson et al., 2019; Grevemeyer et al., 2018). South of our study area, studies reported a significantly thick crust (~15 km thick) and slower velocities than those typical of the oceanic crust compilation, which have been attributed to the presence of the Carnegie Ridge (Gailler et al., 2007; Graindorge et al., 2004; Sallarès et al., 2005). Further North, more typical oceanic crust velocities and thickness were observed (Agudelo et al., 2009; Gailler et al., 2007).

On both trench-perpendicular lines A and E, Vp increases continuously from the trench with depth and distance along the interplate. On Line A, Vp ranges from 4.0 km/s at the trench to 5.7 km/s at 10 km depth (at 50 km DLT). This trend imaged on trench-perpendicular lines is interrupted by two notable exceptions at shallow depths: (a) the Low Vp anomaly on Line A discussed hereafter (LVO), and (b) the outcrop of oceanic crust near the trench on

Figure 8. Vertical velocity gradient for Line E (a), Line A (b), Line 3 (c) and Line 4 (d). Same masks as in Figure 7. Dashed black line represents the interplate from Font et al. (2013). Bold black line on the *X* axis represents the active seismic shots that have been picked along the line. Doted white lines outline the areas of the LVF and LVO. Dashed white lines outline the potential extension of the LVF. Green and red lines are the forearc and the oceanic basement identified in the MCS (HIPER E, 3 and 4 Galve (2020) and SISTEUR 22 Collot (2000)).

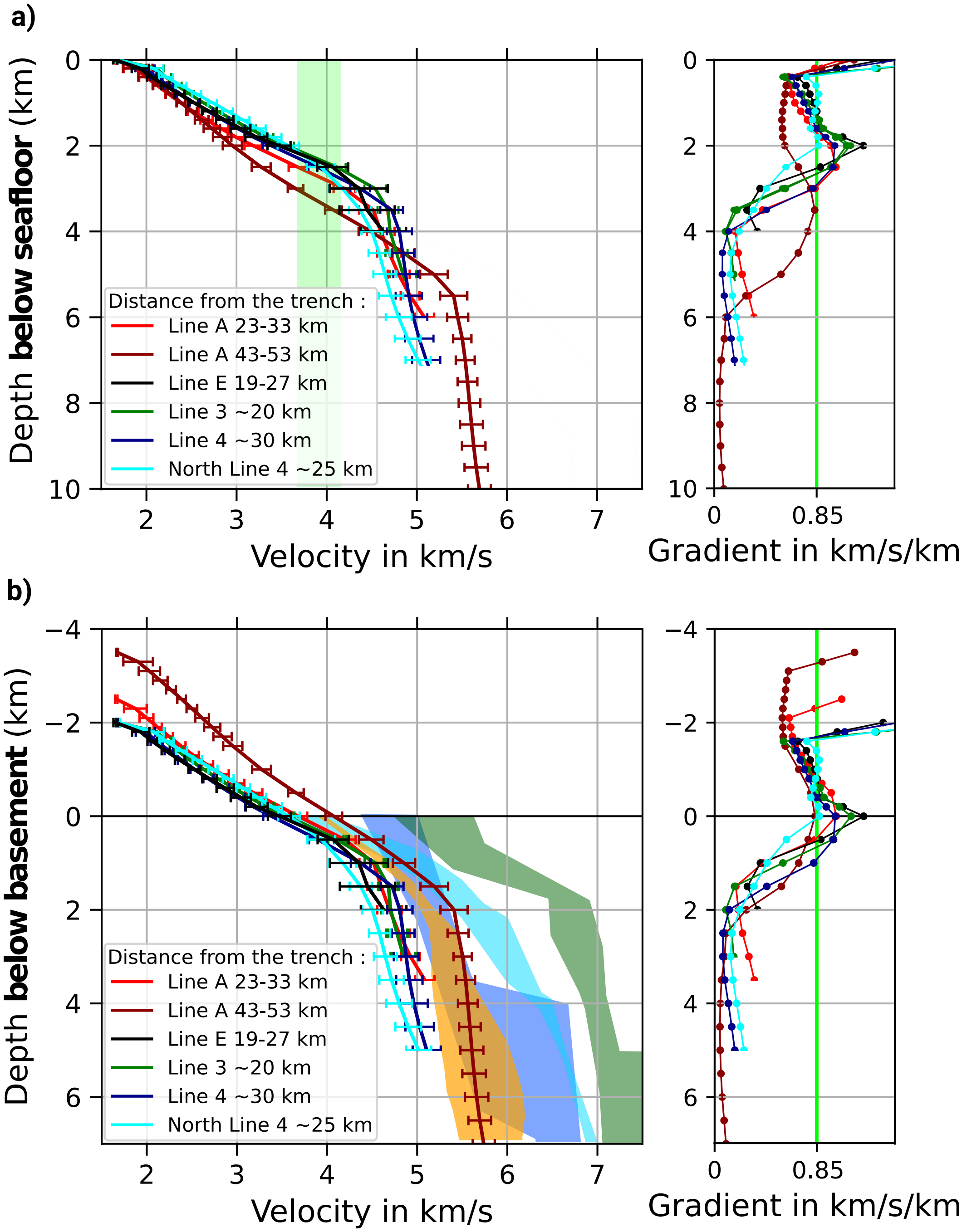

Figure 9. Average 1D Vp model and corresponding Vp gradient in the forearc domain (a) below the seafloor (b) below the basement. Red and brown lines characterize Line A respectively at 23–33 km and 45–53 km from the trench. Black line characterize Line E at 19–27 km from the trench. Green line is for Line 3 located at ~20 km from the trench. Dark and light blue lines characterize Line 4 south and north segment respectively at ~30 and ~25 km from the trench. Light green area in (a) corresponds to the average position of the end of the sedimentary unit as indicated by MCS profiles (HIPER E, 3 and 4 Galve (2020) and SISTEUR 22 Collot (2000)) and the vertical Vp gradient. Light blue area corresponds to Vp on the Carnegie Ridge oceanic crust (Sallarès et al., 2005). Orange area corresponds to a compilation of Vp on the forearc crust in northern Ecuador (García Cano et al., 2014). Dark blue area corresponds to Vp on the Kerguelen oceanic plateau (Operto & Charvis, 1995). Dark green area corresponds to Vp for an oceanic crust compilation (Christeson et al., 2019).

10.1029/2026JB033929

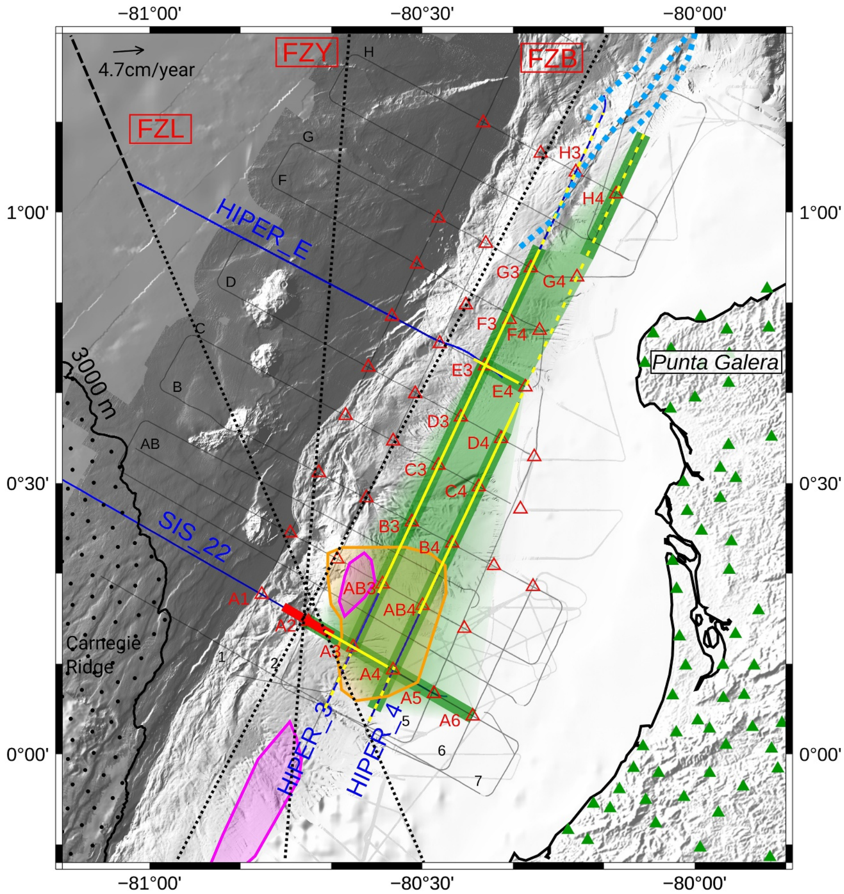

Figure 10. Map view of the 3D forearc structures and position of the proposed fracture zones responsible for LVO anomaly. In blue, MCS profiles from HIPER1 and the SISTEUR experiment (Collot, 2000; Galve, 2020). Offshore, red triangles correspond to OBS and onshore green triangles to land stations. Black line corresponds to the position of shots for the wide-angle seismic acquisition. Thick red line corresponds to the low velocity zone in the oceanic crust (LVO) seen on Line A. Yellow lines and yellow dashed line correspond to the low velocity anomaly in the forearc crust (LVF) seen on Line A, E, 3 and 4. Green area is the 3D extension of the imaged HVVG (high vertical Vp gradient) marking the forearc basement. Blue dashed line corresponds to the position of the Ancon fault from Collot et al. (2008) and extended by Gonzalez (2018); Collot et al. (2025). Black dashed line is the fracture zone from Lonsdale (2005) and black dotted lines correspond to the extension of fracture zones in the area: FZL Extension of a fracture zone from Lonsdale (2005). FZY) Extension of the fracture zone from the Yaquina graben transform fault (Hardy, 1991; Lonsdale, 2005). FZB) Extension and reorientation of a fracture zone coming from the transform fault boarding the Buenaventura extinct rift (Collot et al., 2008; Hardy, 1991). Orange area is the position of the double peaked seamount from Marcaillou et al. (2016). Purple area is the position of A1 (northern area) and A2 anomaly (southern area) from León-Ríos et al. (2021).

Line E. The two trench-parallel lines 3 and 4 confirm these results at the crossing point with trench-perpendicular lines and show their along-trench extent.

On Line A, the low Vp anomaly (LVO) is located between 8 and 19 km, with Vp dropping by 0.5–1.0 km/s compared to the surrounding structure (Figure 7b). The top of the slab was imaged by the MCS SIS22 profile (see "D" reflector in Figure 3 in Marcaillou et al. (2016)) and also delineated by seismicity distribution by Font et al. (2013) (respectively red and black dash lines, Figure 7). Therefore the imaged LVO anomaly is located within the subducting plate and affects the isovelocities from 3.7 km/s down to 7.0 km/s at 15 km depth. The robustness of this anomaly was assessed based on computed standard deviations and checkerboard tests (Figure 6a and Figure S8 in Supporting Information S1), which highlight a well-constrained region with low uncertainties (<0.1 km/s) and a good recovery of 10×5 km anomalies down to 10 km depth. Additional high-resolution tests show the resolution and smearing effects of a low velocity anomaly in this specific area. Results of these tests are available in (Figure S9 in Supporting Information S1) and confirm the good resolution of the anomaly down to at least 10 km depth. Small smearing effect at the top of the anomaly might be responsible for the deepening of the 4.0 km/s contours below the interplate. This LVO anomaly is only imaged on Line A and is absent on Line E (65 km farther north).

6.4. Localized Evidence of Oceanic Moho Depth

Inversion of reflected phases (PmP) was attempted for all seismic lines. However, only a limited number of PmP arrivals could be reliably identified and picked on rather short offset ranges (5–35 km) for a few OBS sections. Joint inversion of the velocity model and Moho topography was performed using the Bayesian approach of tomo2D with the same a priori ranges described in the Methods section. The Moho topography on Line 3 is constrained by crossing rays from direct and reverse shots only between 50 and 60 km model distance (C3 to D3) at a depth of 24.5 km below the sea level (Figure 7c). This leads to an oceanic crustal thickness of ∼17 km in this very localized area. It corresponds to thick oceanic crust which agrees to the known thickness range of the CR crust (14–19 km thick).

7. Discussion

In the following discussion, we interpret the seismic structures described in the results section. We first explore the geometry and nature of the forearc crust. We then interpret the origin of the two low velocity areas in the forearc crust (LVF) and in the subducting oceanic crust (LVO).

7.1. Forearc Crust

7.1.1. Nature and Extent of the Basement

The joinly imaged forearc basement and sedimentary cover offshore northern Ecuador by WAS and MCS HIPER E, 3 and 4 Galve (2020) and SISTEUR 22 Collot (2000) provide new constraints on their nature and geometry along the margin. The highly reflective layer located at the base of the sedimentary layer, above the forearc basement (lower sedimentary (ls) layer in Marcaillou et al. (2016)) is interpreted by Hernández et al. (2020) as the San Eduardo formation. The latter consists of limestone from Early Eocene which is highly reflective due to the presence of carbonate, and that overlies the margin basement. A wide range of velocities is attributed to carbonates depending on sediment porosity and diagenetic alteration, with values reaching highs of 6.5 km/s (Anselmetti & Eberli, 1993; Jeppson & Kitajima, 2022; Kenter et al., 1995). The San Eduardo formation contains carbonate-rich limestone, characterized by significantly higher Vp values in comparison to the surrounding sediments, so it could be responsible of the high vertical velocity gradient (HVVG) on our tomographic model. Then, the maximum vertical Vp gradient value of the HVVG zone is interpreted to mark the top of the forearc crust (Figure 8), which corresponds with the basement as identified on MCS profiles (HIPER E, 3 and 4 Galve (2020) and SISTEUR 22 Collot (2000)). Both of these markers are used to map the spatial extent of the interface between the forearc crust and the sedimentary cover.

The HVVG basement map (Figure 10) highlights a change in the distance from the trench of the trenchward basement boundary off Punta Galera. Concerning the landward basement boundary, it is an acquisition boundary and in no case determines a true limit to the extent of the HVVG forearc basement to the east. Offshore drilling in the Manabi Basin (Hernández et al., 2020) and onshore drilling (Jaillard et al., 2009) have demonstrated the presence of the San Eduardo Formation (50 km further south) suggesting a landward extension of the HVVG.

Along Line A and E, the trenchward boundary of the HVVG basement (Figure 10) is located at ∼15 km DLT. Despite the presence of a reflector closer to the trench at shallower depth below the sea-bottom on MCS profiles HIPER E and SIS 22 (Galve (2020); Marcaillou et al. (2016); Figures 7a, 7b, 8a, and 8b), the absence of HVVG in this frontal part of the inner margin wedge may be linked to the proximity with the trench. The close distance from the deformation front may have increased the fracturation and/or alteration of rocks from the outer margin wedge to the inner margin wedge toe (0–30 km DLT) with greater damage closer to the trench, especially in this context of erosional margin (Christeson et al., 1999; Gailler et al., 2007; García Cano et al., 2014; Krabbenhöft et al., 2004; Ranero & Von Huene, 2000; Sallarès & Ranero, 2005). We also cannot rule out a different sedimentary nature in this area, for example, the absence of the San Eduardo Formation closer to the trench, which could lead to a different velocity structure and to the absence of the HVVG.

The northern termination of the acoustic basement reflector on profile 3 coincides with the termination of the HVVG basement. It also corresponds to the location of the southern initiation of the trench-parallel Ancon Fault zone (Collot et al., 2008, 2025; Gonzalez, 2018). This suggests a landward shift of the HVVG basement compared to Line A and E with a trenchward termination landward of profile 3. As for the frontal part, we cannot exclude the existence of a lateral change in the lower sedimentary unit's nature, that could lead to a smoother vertical gradient in the absence of carbonates. But the presence of this fault zone along profile 3 could also explain the lower velocities in the first 3 km depth by rock fracturing and alteration leading to the absence of the HVVG signature and affecting the reflectivity of the forearc basement.

7.1.2. Nature of Forearc Crust

We compare 1D Vp models extracted along Line A (outside the LVF, at 43–53 km from the trench, profiles A5–A6, Figure 9) with 1D Vp models from previous studies of the northern Ecuadorian margin at comparable distances from the trench (Gailler et al., 2007; García Cano et al., 2014). The results highlight a similar velocity structure, suggesting a similar nature of the forearc crust along northern and central Ecuador. These observations support the interpretation that the forearc crust from northern to central Ecuador shares a common nature. According to previous studies Ecuadorian basement could be made of mafic to ultramafic rocks coming from the accretion of an oceanic terrane to the margin (Gailler et al., 2007; García Cano et al., 2014) with oceanic plateau affinity (Hernández et al., 2024).

7.2. Low Velocity in the Inner Margin Wedge (LVF)

The LVF is situated at the frontal part of the inner margin wedge, within a distance of 15–30 km DLT all along the margin except in the northern part of Line 3 and 4. Since we define the LVF having velocities lower than 5 km/s and we highlight that the margin basement mimics the 4 km/s iso-velocity contour, we can then extrapolate the presence of the LVF in Line 3 and 4 (Dashed white area in Figures 7c, 7d, 8c, and 8d). These LVF areas at both line ends result from the absence of crossing rays, whereas the one in the central part of Line 4 is due to missing shots.

All the 1D Vp models extracted along our four lines in this frontal zone reveal strikingly similar values, with velocities of less than 5.0 km/s down to 4 km depth below the basement (Figure 9b). This represents a 10% Vp reduction compared with measurements outside the LVF. Previous regional studies show similar results of a margin wedge characterized by velocities lower than 5.0 km/s within distances up to 30 km DLT (Figure S13 in Supporting Information S1) (Gailler et al., 2007; García Cano et al., 2014).

Reduced velocity in the frontal part of the inner margin wedge was also observed offshore Costa Rica on the Cocos ridge subduction zone (Martínez-Loriente et al., 2019). They linked this feature to the fracturing and/or alteration of the forearc crust rocks near the trench, causing slower Vp compared to the rest of the forearc crust (Christeson et al., 1999; Krabbenhöft et al., 2004; Ranero & Von Huene, 2000; Sallarès & Ranero, 2005). Therefore, the LVF imaged along the frontal inner margin wedge, except near the Ancon fault zone, is likely produced by the same phenomenon and appears to terminate where the forearc crust becomes thicker and mechanically stronger (Gailler et al., 2007; García Cano et al., 2014) at a distance of ~30 km from the trench (Figure S13 in Supporting Information S1). Comparable low velocity trend in the inner margin wedge has also been reported in other subduction zones, such as in the Lesser Antilles and central Chile (Bangs et al., 2003; Contreras-Reyes et al., 2014; Kopp et al., 2011; Koulakov et al., 2011; Sallarès & Ranero, 2005), suggesting this could be an expected phenomenon in many subduction systems.

7.3. Possible Origins for the Low Velocity Anomaly in the Subducting Oceanic Crust (LVO)

The low velocity anomaly LVO is located in the downgoing plate below the margin on Line A, a few kilometers after the trench. Previous studies on the Ecuadorian margin highlighted a similar Vp anomalies. The origin of this anomaly remains uncertain, and several hypotheses are proposed below.

One option is the presence of a subducted seamount, which could be responsible of the velocity drop in the region. León-Ríos et al. (2021) interpreted the northern piece of an elongated trench-parallel low velocity zone (LVZ named A1, Figure 2) and its associated seismicity, imaged at 10 km NE of our LVO anomaly, as belonging to a >2-km-high subducting volcanic edifice. The slight discrepancy in the location of their A1 anomaly compared with our LVO anomaly could be attributed to the different node definitions used in the two inversion grids. MCS profiles of the SISTEUR survey (SIS22, SIS54 and SIS55 profiles) revealed a spatially coincident structure in

Marcaillou et al. (2016) who mapped its lateral extent in the southern prolongation of the Atacames Seamount Chain (Figure 10). Both anomalies could therefore represent the same crustal feature. Hotspot-generated seamounts usually have lower P-waves velocities in the subseafloor due to low densities and high porosities associated with extrusive lavas with small scale intrusions (Hammer et al., 1994; Warwel et al., 2025; Watts et al., 2021; Weigel & Grevemeyer, 1999; Wessel et al., 2022).

However, two points challenge this interpretation. First, the origin of the Atacames seamount chain remains unknown, and higher Vp than in the surrounding oceanic crust would be expected if these seamounts had a different origin than hotspot-generated ones (Contreras-Reyes et al., 2010; Martínez-Loriente et al., 2019; Nishizawa et al., 2009; Ponce et al., 2025). Second, our imaged LVO anomaly is located 10–15 km trenchward of the seamount flank mapped by the coincident (SIS22) and adjacent MCS profiles by Marcaillou et al. (2016) (Figure 10). Inspection of the oceanic crustal structure on SIS22 profile across the LVO reveals no significant topography or magmatic-type heterogeneity, weakening the seamount hypothesis to explain its origin unless the anomaly reflects the roots of a seamount located offline and therefore not visible on SIS22.

A second option is the effect of bending faults visible in the outer rise in Figure 10, that could also be a possible explanation for the origin of the LVO anomaly. Bending faults can be responsible for the fracturating, increasing porosity, hydration and alteration of the oceanic crust (Grevemeyer et al., 2018; Ivandic et al., 2008; Moscoso & Grevemeyer, 2015). However these studies highlight a velocity drop of only 0.2–0.4 km/s and over a much wider area, extending from the outer rise to the trench, than the localized LVO anomaly. The use of bending faults as a standalone explanation for the LVO is therefore unlikely.

Finally, the presence of a fracture zone (Figure 2), being reactivated by plate bending, could explain all of the above observations. The existence of several fracture zones have been previously highlighted further in the north of our study area (Collot et al., 2008; Hardy, 1991; Lonsdale, 2005; Sallarès & Charvis, 2003), and three of them could be good candidates. A first one presented by Lonsdale (2005), NW of our 2D grid (FZL in Figures 1 and 10), could be extended further SE over a ∼100 km distance up to the LVO anomaly without significant orientation change needed. A second one is proposed by Hardy (1991), called the Minor fossil transform fault, which is associated with the Buenaventura extinct rift segment, located northeast of the Yaquina graben (FZB in Figures 1 and 10). Collot et al. (2008) interpreted a faulted graben imaged by MCS data at the trench at 1°45′N of latitude (Esmeraldas canyon termination) as possibly belonging to this Minor fossil transform fault, implying a 50 km southward extent. A further 160 km southward extension of this fracture zone in a sub-parallel orientation to the trench could match the position of the LVO anomaly (FZB in Figures 1 and 10). Such dimensions are common for fracture zones. One example can be taken in the area with the Panama Fracture Zone which extends for more than 600 km (Peirce et al., 2023). Finally, it is noteworthy that an extinct transform fault is passing along the Yaquina graben (Hardy, 1991; Lonsdale, 2005; Sallarès & Charvis, 2003). As suggested by Sallarès and Charvis (2003), this extinct transform fault could be prolonged by a fracture zone, given that the latter could have played a similar role to the Panama fracture zone, which shifted the Malpelo ridge southwards from the Cocos ridge. It then matches the position of LVO anomaly (FZY in Figures 1 and 10). Previous studies on the Gofar and Clipperton transform faults of the East Pacific Rise highlight a ∼5-km-wide Vp anomaly, with a velocity drop of 0.5–1.5 km/s in the oceanic crust (Roland et al., 2012; Van Avendonk et al., 2001) matching the characteristic of our LVO anomaly. Furthermore, Liu et al. (2023) highlighted Vp/Vs ratio variation along the Gofar transform fault with values matching the Vp/Vs model of León-Ríos et al. (2021) around the LVO. Finally, Contreras-Reyes et al. (2026) constrain Vp and Vp/Vs at the termination of the 85°W Transform fault on the Carnegie ridge, ∼500 km from the trench. They image a Vp/Vs ratio of 1.7–1.8, similar to León-Ríos et al. (2021) ratio along with a decrease of Vp, supporting our interpretation of the LVO anomaly coming from the presence of a fracture zone in our study area of the Carnegie ridge. Studies on fracture zone also highlight remarkable Vp reduction but not as great as on a transform fault.

The LVO anomaly can be explained by the reactivation of the fault by plate bending during the subduction, enhanced by the presence of the 2-km-high CR causing a larger deformation and allowing fluids to circulate. Evidence of stronger reactivation of faults near the CR subduction can be seen on Figure 2 with larger finite throws of bending faults appearing in the bathymetry. If the LVO and A2 anomaly (Figure 2) belong to the same structure, then their alignment suggests FZY or FZB as the most likely candidates, and rules out FZL because it is too oblique.

8. Conclusion

This study used data from the new HIPER2 campaign and applied successfully the Bayesian approach of tomo2D on an active margin filling the existing knowledge gap by providing four new seismic velocity models of the Pedernales margin segment. The joint interpretation of MCS data with our 2D velocity models provide consistent results in the main features showing the robustness of the Bayesian version of tomo2D and helping us to interpret key velocity structures in the northern Ecuadorian margin in 3D.

We find a high vertical Vp gradient anomaly which closely follows MCS interpretation of the forearc basement except in the highly fractured first 15 km DLT. This HVVG is interpreted as potentially coming from a highly reflective limestone layer on top of the basement and corresponding to the San Eduardo formation (Hernández et al., 2020). This marker is absent in the northern part of Line 3, coinciding with the Ancon fault zone indicating a change in the velocity structure.

The forearc crustal low Vp area (LVF) identified 15–30 km DLT within the toe of the inner margin wedge is characterized by Vp values between 4.0 and 5.0 km/s. It is interpreted as resulting from fracturing and alteration of forearc rocks near the trench in an erosional subduction context.

The oceanic crustal low Vp anomaly (LVO) feature, appears ∼5 km DLT within the subducting plate. Three possible origins for this anomaly were examined: a subducted seamount, bending-related faults, and a fossil fracture zone. Among them, the fossil fracture zone provides the most consistent explanation for the observed data.

These results lay the groundwork for more accurate seismic hazard models and future investigations of megathrust behavior in Ecuador. They also provide key information to develop the initial velocity model for the incoming 3D tomographic inversion. The latter will offer improved resolution of the velocity structures in both the forearc and subducting oceanic crust providing crucial information that will contribute to a better understanding of the spatial variations in contrasting slip behaviors observed along the Ecuadorian margin.

Inclusion in Global Research Statement

We thank the Instituto Geofisico de la Escuela Politecnica Nacional for their support and for making resources available for our fieldwork. Our decades-long partnership produces large-scale projects such as the HIPER project. This research was made possible by a specific research agreement between the Instituto Oceanográfico y Antártico de la Armada (INOCAR) in Ecuador and the Institut de la Recherche pour le Développement (IRD) in France. Thanks to the IRD representation and the French Embassy in Quito for their invaluable logistical and material support.

Conflict of Interest

The authors declare no conflicts of interest relevant to this study.

Availability Statement

All MCS data sets from French cruises are available in the French National Marine Database SISMER at Collot (2000) for SISTEUR, Pontoise and Charvis (2005) for Esmeraldas and at Galve (2020, 2022) for HIPER marine campaigns. Data labeled "restricted access" will be made available following a request via an Application Form on the platform after advice of the cruise supervisor conformably to the European and French legislation. All SEGY data sets and associated picks are available at Delsuc et al. (2025). Data will be released after the acceptance of the paper and can be accessed by reviewers at https://radar.kit.edu/radar/en/dataset/edwh9kz9t586hw2k?token=yhfdhtENFvGwEpIrcJua. Requirement for SCAN-2009 seismic data can be addressed to Dirección de Análisis de Información Estratégica de Hidrocarburos Av República de El Salvador N36-64 years Suecia, Quito 170135. Edificio MSP. Piso 5, Ecuador. Figures were made with Matplotlib version 3.8.4 (Hunter, 2007) and Generic Mapping Tools (GMT) version 6 (Wessel et al., 2019). Figures of ocean bottom seismometers sections and picking of first arrivals were made on Shearwater Reveal software version 6.2 using an academic license.

Acknowledgments

This work has been supported by the French government, through the UCAJEDI Investments in the Future project managed by the National Research Agency (ANR) with the reference number ANR-15-IDEX-01. It was also supported by the ANR FLUID2SLIP project, Grant n°ANR-21-CE49-0012 of the French Agence Nationale de la Recherche, the French National Fleet (Ifremer), The Karlsruhe Institute of Technology, the Institut de Recherche pour le Développement (IRD) and the Côte d'Azur Observatory. We thank to the German-Ecuadorian team who deployed and maintained the network of ~100 land stations: Dario Garcia Castillo (IG-EPN), Cristian Viracucha Quinga (IG-EPN), Wilson Acero Quilumbaquin (IG-EPN), Ivan Tapa Caiza (IG-EPN), Lenny Mejia Mendez (KIT), Benedikt Braszus (KIT) and Hans Agurto-Detzel (KIT) as well as the captain and crew of R/V L'Atalante cruise HiPER2. We thank the OBS team for efficiently managing multiple deployments of the instruments: Pascal Pelleau (Ifremer), Anthony Ferrant (Ifremer), Eduardo Soto (Géoazur) and Davide Oregioni (Géoazur). We would like to thank the Secretaria de Hydrocarburos del Ecuador (SHE) for providing seismic sections from the SCAN-2009 seismic experiment. We thank Shearwater Geoservices for providing an academic license to use the Reveal seismic processing software. We thank Jun Korenaga for his help adaptating bayesian approach of tomo2d to our data set. We thank the editor Fenglin Niu, the associate editor, Valenti Sallarès and one anonymous reviewers for helpful comments that improved the manuscript. Open access publication funding provided by COUPERIN CY26.

References

Acquisto, T., Bécel, A., Singh, S. C., & Carton, H. (2022). Evidence of strong upper oceanic crustal hydration outboard the Alaskan and Sumatran subduction zones. *Journal of Geophysical Research: Solid Earth*, *127*(10), e2022JB024751. https://doi.org/10.1029/2022JB024751

Agudelo, W., Ribodetti, A., Collot, J. Y., & Operto, S. (2009). Joint inversion of multichannel seismic reflection and wide-angle seismic data: Improved imaging and refined velocity model of the crustal structure of the north Ecuador–south Colombia convergent margin. *Journal of Geophysical Research*, *114*(B2), 2008JB005690. https://doi.org/10.1029/2008JB005690

Agurto-Detzel, H., Font, Y., Charvis, P., Régnier, M., Rietbrock, A., Ambrois, D., et al. (2019). Ridge subduction and afterslip control aftershock distribution of the 2016 Mw 7.8 Ecuador earthquake. *Earth and Planetary Science Letters*, *520*, 63–76. https://doi.org/10.1016/j.epsl.2019.05.029

Anselmetti, F. S., & Eberli, G. P. (1993). Controls on sonic velocity in carbonates. *Pure and Applied Geophysics*, *141*(2–4), 287–323. https://doi.org/10.1007/BF00998333

Bangs, N. L., Christeson, G. L., & Shipley, T. H. (2003). Structure of the lesser antilles subduction zone backstop and its role in a large accretionary system. *Journal of Geophysical Research*, *108*(B7). https://doi.org/10.1029/2002JB002040

Barnes, P. M., Wallace, L. M., Saffer, D. M., Bell, R. E., Underwood, M. B., Fagereng, A., et al. (2020). Slow slip source characterized by lithological and geometric heterogeneity. *Science Advances*, *6*(13), eaay3314. https://doi.org/10.1126/sciadv.aay3314

Bassett, D., Arnulf, A., Henrys, S., Barker, D., Van Avendonk, H., Bangs, N., et al. (2022). Crustal structure of the Hikurangi margin from SHIRE seismic data and the relationship between forearc structure and shallow megathrust slip behavior. *Geophysical Research Letters*, *49*(2), e2021GL096960. https://doi.org/10.1029/2021GL096960

Chalumeau, C., Agurto-Detzel, H., De Barros, L., & Charvis, P., & the Rapid Response Team of the 2016 Pedernales Earthquake. (2023). Spatio-temporal evolution of aftershock and repeater source properties after the 2016 Pedernales earthquake (Ecuador). *Journal of Geophysical Research: Solid Earth*, *128*(2), e2022JB025353. https://doi.org/10.1029/2022JB025353

Christeson, G. L., McIntosh, K. D., Shipley, T. H., Flueh, E. R., & Goedde, H. (1999). Structure of the Costa Rica convergent margin, offshore Nicoya Peninsula. *Journal of Geophysical Research*, *104*(B11), 25443–25468. https://doi.org/10.1029/1999JB900251

Christeson, G. L., Goff, J. A., & Reece, R. S. (2019). Synthesis of oceanic crustal structure from two-dimensional seismic profiles. *Reviews of Geophysics*, *57*(2), 504–529. https://doi.org/10.1029/2019RG000641

Collot, J. Y. (2000). Sisteur cruise. RV Le Nadir. https://doi.org/10.17600/80050

Collot, J. Y., Agudelo, W., Ribodetti, A., & Marcaillou, B. (2008). Origin of a crustal splay fault and its relation to the seismogenic zone and underplating at the erosional north Ecuador–south Colombia oceanic margin. *Journal of Geophysical Research*, *113*(B12), 2008JB005691. https://doi.org/10.1029/2008JB005691

Collot, J. Y., Charvis, P., Gutscher, M., & Operto, S. (2002). Exploring the Ecuador-Colombia active margin and interplate seismogenic zone. *EOS Transactions of the American Geophysical Union*, *83*(17), 185–190. https://doi.org/10.1029/2002EO000120

Collot, J. Y., Michaud, F., Alvarado, A., Marcaillou, B., Sosson, M., Ratzov, G., et al. (2009). Visión general de la morfología submarina del margen convergente de ecuador-sur de colombia: Implicaciones sobre la transferencia de masa y la edad de la subducción de la cordillera de carnegie. *Geologia y geofisica marina y terrestre del Ecuador: desde la costa continental hasta las Islas Galápagos*, 47–74.

Collot, J. Y., Migeon, S., Spence, G., Legonidec, Y., Marcaillou, B., Schneider, J.-L., et al. (2005). Seafloor margin map helps in understanding subduction earthquakes. *EOS Transactions of the American Geophysical Union*, *86*(46), 463–465. https://doi.org/10.1029/2005EO460003

Collot, J. Y., Proust, J., Nocquet, J., Martillo, C., Michaud, F., Lebrun, J., et al. (2022). From long-to short-term inter-plate coupling at the subducted Carnegie ridge crest, offshore central Ecuador. *Journal of Geophysical Research: Solid Earth*, *127*(8), e2022JB024192. https://doi.org/10.1029/2022JB024192

Collot, J. Y., Ratzov, G., Michaud, F., Galve, A., Proust, J.-N., Gonzalez, M., et al. (2025). A possible tsunamigenic near-trench strike-slip fault, offshore north ecuador–south Colombia. *Journal of Geophysical Research: Solid Earth*, *130*(12), e2024JB030779. https://doi.org/10.1029/2024JB030779

Contreras-Reyes, E., Becerra, J., Kopp, H., Reichert, C., & Díaz-Naveas, J. (2014). Seismic structure of the north-central chilean convergent margin: Subduction erosion of a paleomagmatic arc. *Geophysical Research Letters*, *41*(5), 1523–1529. https://doi.org/10.1002/2013GL058729

Contreras-Reyes, E., Grevemeyer, I., Watts, A., Planert, L., Flueh, E., & Peirce, C. (2010). Crustal intrusion beneath the Louisville hotspot track. *Earth and Planetary Science Letters*, *289*(3–4), 323–333. https://doi.org/10.1016/j.epsl.2009.11.020

Contreras-Reyes, E., Obando-Orrego, S., Maksymowicz, A., Grevemeyer, I., & Utrera, C. (2026). Vp/vs ratios, density structure, and lithospheric flexure of the carnegie and malpelo ridges: Insights into Panama basin tectonic evolution and galapagos hotspot magmatism. *Gondwana Research*.

Delsuc, A., Galve, A., Laigle, M., Rietbrock, A., Schenini, L., Agurto-Detzel, H., et al. (2025). Characterizing the forearc basement and subducting structures of the northern Ecuadorian margin [Dataset]. *radar kit*. https://doi.org/10.35097/edwh9kz9t586hw2k

Evain, M., Galve, A., Charvis, P., Laigle, M., Kopp, H., Bécel, A., et al. (2013). Structure of the Lesser Antilles subduction forearc and backstop from 3D seismic refraction tomography. *Tectonophysics*, *603*, 55–67. https://doi.org/10.1016/j.tecto.2011.09.021

Font, Y., Segovia, M., Vaca, S., & Theunissen, T. (2013). Seismicity patterns along the Ecuadorian subduction zone: New constraints from earthquake location in a 3-D a priori velocity model. *Geophysical Journal International*, *193*(1), 263–286. https://doi.org/10.1093/gji/ggs083

Gailler, A., Charvis, P., & Flueh, E. R. (2007). Segmentation of the Nazca and South American plates along the Ecuador subduction zone from wide angle seismic profiles. *Earth and Planetary Science Letters*, *260*(3–4), 444–464. https://doi.org/10.1016/j.epsl.2007.05.045

Galve, A. (2020). *Hiper cruise*. RV L'Atalante. https://doi.org/10.17600/18001348

Galve, A. (2022). Hiper (suite) cruise. *RV L'Atalante*. https://doi.org/10.17600/18002493

García Cano, L. C., Galve, A., Charvis, P., & Marcaillou, B. (2014). Three-dimensional velocity structure of the outer fore arc of the Colombia-Ecuador subduction zone and implications for the 1958 megathrust earthquake rupture zone. *Journal of Geophysical Research: Solid Earth*, *119*(2), 1041–1060. https://doi.org/10.1002/2012JB009978

Gonzalez, M. (2018). Nature and origin of sedimentary deposits in the Ecuador subduction trench: Paleoseismological implications. (Doctoral dissertation, Université de Rennes). Retrieved from https://theses.hal.science/tel-02173709v1

Graindorge, D., Calahorrano, A., Charvis, P., Collot, J., & Bethoux, N. (2004). Deep structures of the Ecuador convergent margin and the Carnegie Ridge, possible consequence on great earthquakes recurrence interval. *Geophysical Research Letters*, *31*(4), 2003GL018803. https://doi.org/10.1029/2003GL018803

Grevemeyer, I., Ranero, C. R., & Ivandic, M. (2018). Structure of oceanic crust and serpentinization at subduction trenches. *Geosphere*, *14*(2), 395–418. https://doi.org/10.1130/GES01537.1

Hammer, P. T. C., Dorman, L. M., Hildebrand, J. A., & Cornuelle, B. D. (1994). Jasper seamount structure: Seafloor seismic refraction tomography. *Journal of Geophysical Research*, *99*(B4), 6731–6752. https://doi.org/10.1029/93JB02170

Hardy, N. (1991). Tectonic evolution of the easternmost Panama basin: Some new data and inferences. *Journal of South American Earth Sciences*, *4*(3), 261–269. https://doi.org/10.1016/0895-9811(91)90035-J

Hayes, G. P., Moore, G. L., Portner, D. E., Hearne, M., Flamme, H., Furtney, M., & Smoczyk, G. M. (2018). Slab2, a comprehensive subduction zone geometry model. *Science*, *362*(6410), 58–61. https://doi.org/10.1126/science.aat4723

Hayes, G. P., Wald, D. J., & Johnson, R. L. (2012). Slab1.0: A three-dimensional model of global subduction zone geometries. *Journal of Geophysical Research*, *117*(B1), 2011JB008524. https://doi.org/10.1029/2011JB008524

Hernández, M. J., Michaud, F., Collot, J.-Y., d'Acremont, E., Proust, J.-N., & Barba, D. (2024). Evolution of the Manabí forearc basin in Ecuador: From the collision of Caribbean oceanic plateau to the build up of the Andes and Coastal Cordilleras. *Tectonophysics*, *870*, 230133. https://doi.org/10.1016/j.tecto.2023.230133

Hernández, M. J., Michaud, F., Collot, J.-Y., Proust, J.-N., & d'Acremont, E. (2020). Evolution of the Ecuador offshore nonaccretionary-type forearc basin and margin segmentation. *Tectonophysics*, *781*, 228374. https://doi.org/10.1016/j.tecto.2020.228374

Hunter, J. D. (2007). Matplotlib: A 2d graphics environment. *Computing in Science & Engineering*, *9*(3), 90–95. https://doi.org/10.1109/MCSE.2007.55

Ivandic, M., Grevemeyer, I., Berhorst, A., Flueh, E. R., & McIntosh, K. (2008). Impact of bending related faulting on the seismic properties of the incoming oceanic plate offshore of Nicaragua. *Journal of Geophysical Research*, *113*(B5), 2007JB005291. https://doi.org/10.1029/2007JB005291

Jaillard, E., Lapierre, H., Ordoñez, M., Álava, J. T., Amórtegui, A., & Vanmelle, J. (2009). Accreted oceanic terranes in Ecuador: Southern edge of the Caribbean Plate? *Geological Society*, *328*, 469–485. https://doi.org/10.1144/SP328.19

Jeppson, T. N., & Kitajima, H. (2022). Velocity-porosity relations in carbonate and siliciclastic subduction zone input materials. *Geochemistry, Geophysics, Geosystems*, *23*(1), e2021GC010074. https://doi.org/10.1029/2021GC010074

Kanamori, H., & McNally, K. C. (1982). Variable rupture mode of the subduction zone along the Ecuador-Colombia coast. *Bulletin of the Seismological Society of America*, *72*(4), 1241–1253. (Publisher: The Seismological Society of America).

Kenter, J. A. M., Ivanov, M., Winterer, E. L., & Sager, W. W. (1995). Parameters controlling acoustic properties of carbonate and volcaniclastic sediments at sites 866 and 869. In *Proceedings of the Ocean drilling Program, scientific results* (Vol. 143, pp. 287–303). Ocean Drilling Program College Station. https://doi.org/10.2973/odp.proc.sr.143.232.1995

Kopp, H., Weinzierl, W., Becel, A., Charvis, P., Evain, M., Flueh, E. R., et al. (2011). Deep structure of the central lesser antilles island arc: Relevance for the formation of continental crust. *Earth and Planetary Science Letters*, *304*(1–2), 121–134. https://doi.org/10.1016/j.epsl.2011.01.024

Korenaga, J., Holbrook, W. S., Kent, G. M., Kelemen, P. B., Detrick, R. S., Larsen, H., et al. (2000). Crustal structure of the southeast Greenland margin from joint refraction and reflection seismic tomography. *Journal of Geophysical Research*, *105*(B9), 21591–21614. https://doi.org/10.1029/2000JB900188

Korenaga, J., & Sager, W. W. (2012). Seismic tomography of Shatsky Rise by adaptive importance sampling. *Journal of Geophysical Research*, *117*(B8), 2012JB009248. https://doi.org/10.1029/2012JB009248

Koulakov, I., Kopp, H., & Stupina, T. (2011). Finding a realistic velocity distribution based on iterating forward modelling and tomographic inversion. *Geophysical Journal International*, *186*(1), 349–358. https://doi.org/10.1111/j.1365-246X.2011.05034.x

Krabbenhöft, A., Bialas, J., Kopp, H., Kukowski, N., & Hübscher, C. (2004). Crustal structure of the Peruvian continental margin from wide-angle seismic studies. *Geophysical Journal International*, *159*(2), 749–764. https://doi.org/10.1111/j.1365-246X.2004.02425.x

León-Ríos, S., Bie, L., Agurto-Detzel, H., Rietbrock, A., Galve, A., Alvarado, A., et al. (2021). 3D local earthquake tomography of the ecuadorian margin in the source area of the 2016 Mw 7.8 Pedernales earthquake. *Journal of Geophysical Research: Solid Earth*, *126*(3), e2020JB020701. https://doi.org/10.1029/2020JB020701

Liu, T., Gong, J., Fan, W., & Lin, G. (2023). In-situ vp/vs reveals fault-zone material variation at the westernmost Gofar transform fault, east Pacific rise. *Journal of Geophysical Research: Solid Earth*, *128*(3), e2022JB025310. https://doi.org/10.1029/2022JB025310

Lonsdale, P. (2005). Creation of the Cocos and Nazca plates by fission of the Farallon plate. *Tectonophysics*, *404*(3–4), 237–264. https://doi.org/10.1016/j.tecto.2005.05.011

Marcaillou, B. (2003). Régimes tectoniques et thermiques de la marge Nord Equateur-Sud Colombie (0°-3, 5° N)-: implications sur la sismogenèse. (PhD Thesis, Paris 6). Retrieved from https://www.documentation.ird.fr/hor/fdi:010053327

Marcaillou, B., Collot, J.-Y., Ribodetti, A., d'Acremont, E., Mahamat, A.-A., & Alvarado, A. (2016). Seamount subduction at the North-Ecuadorian convergent margin: Effects on structures, inter-seismic coupling and seismogenesis. *Earth and Planetary Science Letters*, *433*, 146–158. https://doi.org/10.1016/j.epsl.2015.10.043

Martínez-Loriente, S., Sallarès, V., R. Ranero, C. B., Ruh, J., Barckhausen, U., Grevemeyer, I., & Bangs, N. (2019). Influence of incoming plate relief on overriding plate deformation and earthquake nucleation: Cocos Ridge subduction (Costa Rica). *Tectonics*, *38*(12), 4360–4377. https://doi.org/10.1029/2019TC005586

Moscoso, E., & Grevemeyer, I. (2015). Bending-related faulting of the incoming oceanic plate and its effect on lithospheric hydration and seismicity: A passive and active seismological study offshore Maule, Chile. *Journal of Geodynamics*, *90*, 58–70. https://doi.org/10.1016/j.jog.2015.06.007

Nishizawa, A., Kaneda, K., Watanabe, N., & Oikawa, M. (2009). Seismic structure of the subducting seamounts on the trench axis: Erimo Seamount and Daiichi-Kashima Seamount, northern and southern ends of the Japan Trench. *Earth Planets and Space*, *61*(3), e5–e8. https://doi.org/10.1186/BF03352912

Nocquet, J.-M., Villegas-Lanza, J. C., Chlieh, M., Mothes, P. A., Rolandone, F., Jarrin, P., et al. (2014). Motion of continental slivers and creeping subduction in the northern Andes. *Nature Geoscience*, *7*(4), 287–291. https://doi.org/10.1038/ngeo2099

Operto, S., & Charvis, P. (1995). Kerguelen plateau: A volcanic passive margin fragment? *Geology*, *23*(2), 137–140. https://doi.org/10.1130/0091-7613(1995)023⟨0137:KPAVPM⟩2.3.CO;2

Parra, H., Benito, M. B., & Gaspar-Escribano, J. M. (2016). Seismic hazard assessment in continental Ecuador. *Bulletin of Earthquake Engineering*, *14*(8), 2129–2159. https://doi.org/10.1007/s10518-016-9906-7

Pedoja, K., Dumont, J., Lamothe, M., Ortlieb, L., Collot, J. Y., Ghaleb, B., et al. (2006). Plio-Quaternary uplift of the Manta Peninsula and La Plata Island and the subduction of the Carnegie Ridge, central coast of Ecuador. *Journal of South American Earth Sciences*, *22*(1–2), 1–21. https://doi.org/10.1016/j.jsames.2006.08.003

Peirce, C., Tedd, J., & Hobbs, R. (2023). Structure and dynamics of the Ecuador fracture zone, Panama basin. *Geophysical Journal International*, *235*(2), 1519–1540. https://doi.org/10.1093/gji/ggad315

Ponce, G., Meltzer, A., Wickham-Piotrowski, A., Hoskins, M., Beck, S., Ruiz, M., et al. (2025). Insights into subduction zone complexity in the northern ecuadorian forearc from 3-d local earthquake tomography. *Geophysical Journal International*, *242*(2), ggaf189. https://doi.org/10.1093/gji/ggaf189

Pontoise, B., & Charvis, P. (2005). *Esmeraldas cruise*. RV L'Atalante. https://doi.org/10.17600/5010020

Ranero, C. R., & Von Huene, R. (2000). Subduction erosion along the Middle America convergent margin. *Nature*, *404*(6779), 748–752. https://doi.org/10.1038/35008046

Ratzov, G., Collot, J.-Y., Sosson, M., & Migeon, S. (2010). Mass-transport deposits in the northern Ecuador subduction trench: Result of frontal erosion over multiple seismic cycles. *Earth and Planetary Science Letters*, *296*(1–2), 89–102. https://doi.org/10.1016/j.epsl.2010.04.048

Reynaud, C., Jaillard, E., Lapierre, H., Mamberti, M., & Mascle, G. H. (1999). Oceanic plateau and island arcs of southwestern Ecuador: Their place in the geodynamic evolution of northwestern South America. *Tectonophysics*, *307*(3–4), 235–254. https://doi.org/10.1016/S0040-1951(99)00099-2

Roland, E., Lizarralde, D., McGuire, J. J., & Collins, J. A. (2012). Seismic velocity constraints on the material properties that control earthquake behavior at the quebrada-discovery-gofar transform faults, East Pacific Rise. *Journal of Geophysical Research*, *117*(B11), 2012JB009422. https://doi.org/10.1029/2012JB009422

Rolandone, F., Nocquet, J.-M., Mothes, P. A., Jarrin, P., Vallée, M., Cubas, N., et al. (2018). Areas prone to slow slip events impede earthquake rupture propagation and promote afterslip. *Science Advances*, *4*(1), eaao6596. https://doi.org/10.1126/sciadv.aao6596

Sallarès, V., & Charvis, P. (2003). Crustal thickness constraints on the geodynamic evolution of the galapagos volcanic province. *Earth and Planetary Science Letters*, *214*(3–4), 545–559. https://doi.org/10.1016/S0012-821X(03)00373-X

Sallarès, V., Charvis, P., Flueh, E. R., & Bialas, J., & the SALIERI Scientific Party. (2005). Seismic structure of the Carnegie ridge and the nature of the Galápagos hotspot. *Geophysical Journal International*, *161*(3), 763–788. https://doi.org/10.1111/j.1365-246X.2005.02592.x

Sallarès, V., & Ranero, C. R. (2005). Structure and tectonics of the erosional convergent margin off Antofagasta, north Chile (23 30′ S). *Journal of Geophysical Research*, *110*(B6), 2004JB003418. https://doi.org/10.1029/2004JB003418

Sallarès, V., & Ranero, C. R. (2019). Upper-plate rigidity determines depth-varying rupture behaviour of megathrust earthquakes. *Nature*, *576*(7785), 96–101. https://doi.org/10.1038/s41586-019-1784-0

Seher, T., Singh, S. C., Crawford, W. C., & Escartín, J. (2010). Upper crustal velocity structure beneath the central Lucky Strike Segment from seismic refraction measurements. *Geochemistry, Geophysics, Geosystems*, *11*(5), 2009GC002894. https://doi.org/10.1029/2009GC002894

Sennson, J. L., & Beck, S. L. (1996). Historical 1942 Ecuador and 1942 Peru subduction earthquakes and earthquake cycles along Colombia-Ecuador and Peru subduction segments. *Pure and Applied Geophysics*, *146*(1), 67–101. https://doi.org/10.1007/BF00876670

Vaca, S., Vallée, M., Nocquet, J.-M., Battaglia, J., & Régnier, M. (2018). Recurrent slow slip events as a barrier to the northward rupture propagation of the 2016 Pedernales earthquake (Central Ecuador). *Tectonophysics*, *724–725*, 80–92. https://doi.org/10.1016/j.tecto.2017.12.012

Van Avendonk, H. J. A., Harding, A. J., Orcutt, J. A., & McClain, J. S. (2001). Contrast in crustal structure across the Clipperton transform fault from travel time tomography. *Journal of Geophysical Research*, *106*(B6), 10961–10981. https://doi.org/10.1029/2000JB900459

Wang, K., & Bilek, S. L. (2014). Invited review paper: Fault creep caused by subduction of rough seafloor relief. *Tectonophysics*, *610*, 1–24. https://doi.org/10.1016/j.tecto.2013.11.024

Warwel, A., Lange, D., Dannowski, A., Contreras-Reyes, E., Klaucke, I., Diaz-Naveas, J., et al. (2025). Seismic structure and tectonics of the North-Central Chilean subduction zone along the Copiapó Ridge from amphibious seismic refraction tomography and local seismicity. *Geochemistry, Geophysics, Geosystems*, *26*(1), e2024GC011829. https://doi.org/10.1029/2024GC011829

Watts, A. B., Grevemeyer, I., Shillington, D. J., Dunn, R. A., Boston, B., & Gómez De La Peña, L. (2021). Seismic structure, gravity anomalies and flexure along the Emperor seamount chain. *Journal of Geophysical Research: Solid Earth*, *126*(3), e2020JB021109. https://doi.org/10.1029/2020JB021109

Weigel, W., & Grevemeyer, I. (1999). The Great Meteor seamount: Seismic structure of a submerged intraplate volcano. *Journal of Geodynamics*, *28*(1), 27–40. https://doi.org/10.1016/S0264-3707(98)00030-1

Wessel, P., Luis, J. F., Uieda, L. a., Scharroo, R., Wobbe, F., Smith, W. H., & Tian, D. (2019). The generic mapping tools version 6. *Geochemistry, Geophysics, Geosystems*, *20*(11), 5556–5564. https://doi.org/10.1029/2019GC008515

Wessel, P., Watts, A. B., Kim, S.-S., & Sandwell, D. T. (2022). Models for the evolution of seamounts. *Geophysical Journal International*, *231*(3), 1898–1916. https://doi.org/10.1093/gji/ggac285

Ye, L., Kanamori, H., Avouac, J.-P., Li, L., Cheung, K. F., & Lay, T. (2016). The 16 April 2016, mw 7.8 (ms 7.5) Ecuador earthquake: A quasi-repeat of the 1942 ms 7.5 earthquake and partial re-rupture of the 1906 ms 8.6 Colombia–Ecuador earthquake. *Earth and Planetary Science Letters*, *454*, 248–258. https://doi.org/10.1016/j.epsl.2016.09.006

Yoshimoto, M., Kumagai, H., Acero, W., Ponce, G., Vásconez, F., Arrais, S., et al. (2017). Depth-dependent rupture mode along the Ecuador-Colombia subduction zone. *Geophysical Research Letters*, *44*(5), 2203–2210. https://doi.org/10.1002/2016GL071929

Yuan, X., Korenaga, J., Holbrook, W. S., & Kelemen, P. B. (2020). Crustal structure of the Greenland-Iceland ridge from joint refraction and reflection seismic tomography. *Journal of Geophysical Research: Solid Earth*, *125*(7), e2020JB019847. https://doi.org/10.1029/2020JB019847

Zelt, C. A., & Barton, P. J. (1998). Three-dimensional seismic refraction tomography: A comparison of two methods applied to data from the faeroe basin. *Journal of Geophysical Research*, *103*(B4), 7187–7210. https://doi.org/10.1029/97JB03536